Biomaterials Science

ROYAL SOCIETY OF CHEMISTRY

PAPER

View Article Online
View Journal | View Issue

Cite this: *Biomater. Sci.*, 2026, **14**, 2334

Bioactive chitosan scaffolds reinforced with hydroxyapatite and nickel tungstate for bone tissue engineering

Giovanna A. Grasser,[a] Diana Gabriela Nina Nina,[b] Karolyne dos Santos Jorge Sousa,[b] Mirian Bonifácio,[b] Renata Neves Granito,[b] Ailton José Moreira,[c] Ana Claudia Muniz Rennó,[b] Elson Longo[a] and Marcelo Assis *[b]

Current bone tissue engineering (BTE) scaffolds often fail to simultaneously provide adequate mechanical performance, controlled ion release, and multifunctional biological activity, particularly when incorporating inorganic antimicrobial agents that may induce cytotoxic effects. Addressing this limitation requires bioactive additives capable of modulating cellular responses without compromising structural integrity. In this work, chitosan/hydroxyapatite composite scaffolds produced by freeze-drying were functionalized with $NiWO_4$ nanoparticles for BTE. Hydroxyapatite was incorporated at 10 wt%, while $NiWO_4$ was added at 2.5, 5, and 10 wt%. Structural analyses confirmed that the incorporation of inorganic phases did not induce structural changes in the polymeric matrix. However, thermal analyses revealed that these fillers modulated chitosan–water interactions, promoting a morphological transition from lamellar structures to a more interconnected porous network, which directly impacted the mechanical properties of the scaffolds. Ion release studies showed that $NiWO_4$ did not affect Ca^{2+} leaching, whereas Ni^{2+} release was enhanced by hydroxyapatite at higher $NiWO_4$ contents. Biological assays using MC3T3-E1 and L929 cells indicated cytotoxicity only for scaffolds containing 10 wt% $NiWO_4$ after 14 days. Although $NiWO_4$ induced elevated intracellular oxidative stress within the first 24 h, this effect was mitigated over time, particularly at lower concentrations. The scaffold containing 2.5 wt% $NiWO_4$ synergistically enhanced MC3T3-E1 migration, osteogenic differentiation, and mineral deposition, while hydroxyapatite improved cell adhesion. Additionally, $NiWO_4$ imparted antimicrobial activity, achieving up to 90% bacterial reduction against *E. coli* and *S. aureus via* controlled Ni^{2+} release and ROS generation. Overall, this hybrid scaffold represents a promising platform for BTE.

Received 26th January 2026,
Accepted 23rd March 2026

DOI: 10.1039/d6bm00120c

rsc.li/biomaterials-science

1. Introduction

The development of synthetic substitutes for the repair of critical tissue damage remains one of the greatest challenges at the intersection of materials science and bioengineering.[1] In this scenario, bone tissue engineering (BTE) has emerged as a specialized field focused on the development of bioactive scaffolds with tissue-specific properties designed to overcome the limitations of current clinical treatments.[2] The effectiveness of the scaffolds depends not only on the chemical composition of the material, but also on an architectural design that ensures adequate mechanical properties, controlled porosity and interconnectivity.[3] This structural organization is fundamental to providing the necessary topographic and biochemical stimuli for cellular response, coordinating the processes of adhesion, proliferation, and osteogenic differentiation, which are key points for neovascularization and functional osteogenesis.[4]

The use of composite-based scaffolds is a highly promising strategy for BTE, especially when formed by a polymer matrix incorporating bioactive particles.[5] This combination allows mimicking the hybrid nature of bone tissue, uniting the ease of processing of polymers with the optimization of mechanical properties and the bioactivity conferred by functional fillers. The success of these structures is linked to the biofabrication process employed, and in this scenario, freeze-drying emerges as a common and highly reproducible technique, guaranteeing

[a]*Center for the Development of Functional Materials (CDMF), Universidade Federal de São Carlos (UFSCar), São Carlos, São Paulo, Brazil*
[b]*Department of Biosciences, Federal University of São Paulo (UNIFESP), Santos, São Paulo, Brazil. E-mail: marcelostassis@gmail.com*
[c]*São Paulo State University (UNESP), Institute of Chemistry, Araraquara, São Paulo, Brazil*

rigorous structural control over the scaffold architecture.[6–8] According to Angraini *et al.*, this method enables mechanical performance capable of providing both structural support and the physical stimuli necessary to modulate cell behavior.[9] The integration between pore architecture, biocompatibility, and mechanical stability establishes a microenvironment favorable to cell–matrix interactions and osteogenic differentiation, fundamental requirements in the design of scaffolds aimed at bone regeneration.[10]

Chitosan, due to its biological and ease of processing properties, has been extensively studied as a polymeric matrix in BTE.[11] The advantages that chitosan offers include being naturally sourced and highly biocompatible and biodegradable, besides the ease with which it can be modified, thus permitting safe interaction with biological systems.[12–14] Its chemical functionality and cationic characteristics enable interactions with cells and biomolecules, thereby enhancing cellular responses and bone matrix mineralization.[15] However, when used alone, chitosan may not provide sufficient structural stability and biological cues to fully support complex bone regeneration processes.[16] To address these limitations, composite strategies have been widely explored, aiming to tailor both structural stability and biological functionality through the incorporation of inorganic phases.[17] Piszko *et al.* highlighted that obtaining chitosan composites with hydroxyapatite enhances bioactivity and cell permeability, contributing to improved osteogenic performance.[18]

Hydroxyapatite represents 60–65% of the inorganic composition of bones, being a key material for BTE.[19] Due to its elemental and structural similarity to the mineral phase of bone, hydroxyapatite exhibits unique biological properties, notably its biocompatibility, osteoconductivity, and lack of immune response. These attributes favor cell adhesion, osteoblast proliferation, and mesenchymal stem cell differentiation, consolidating its application in grafts and scaffolds.[20–23] However, the biological performance of hydroxyapatite contrasts with its mechanical limitations, such as low fracture toughness and inherent fragility, which restrict its isolated use in load-bearing sites. Thus, in hybrid scaffolds, hydroxyapatite is mainly employed as a bioactive phase to stimulate cellular responses and mineralization processes, while mechanical performance depends predominantly on scaffold architecture and polymer–ceramic interactions. In this context, the structuring of hybrid systems aims to combine the bioactivity of hydroxyapatite with the structural support provided by polymeric matrices. Moreover, the incorporation of functional inorganic phases has been explored as a strategy to introduce additional functionalities. Silva *et al.* obtained hydroxyapatite heterostructures with $AgVO_3$, making this composite antibacterial against *Staphylococcus aureus*, one resistant (MRSA) and one susceptible to methicillin (MSSA), in addition to acquiring bluish white-light luminescence emissions.[24] Zhou *et al.* demonstrated that coatings based on Zn-doped HA provide a protective barrier against corrosion alongside promoting potent antibacterial activity and osteogenic potential.[25] Thus, these hybrid systems expand the functional potential of hydroxyapatite-based scaffolds by introducing therapeutic functionalities beyond their inherent bioactivity.[26,27]

Building upon the strategy of incorporating functional inorganic phases, nickel (Ni)-based materials have attracted interest as promising candidates in BTE. Although Ni requires attention regarding safety at high concentrations, its biological effects are strictly dose-dependent; at trace levels, Ni^{2+} ions participate in essential biochemical processes, suggesting a relevant biological role when properly controlled.[28,29] Horie *et al.* demonstrated that the cytotoxicity threshold induced by Ni^{2+} ions was approximately 50 μg mL^{-1} (~0.386 mM).[30] While Ti-based materials are widely recognized for their long-term biocompatibility yet remain largely bioinert,[31] and Cu-based systems provide pronounced antimicrobial activity but are highly dependent on release kinetics,[32] Ni-based materials occupy an intermediate position in which biological modulation can be achieved through strict dose control.

This duality allows Ni to be explored not only for structural reinforcement but also as a modulator of cellular response, paving the way for the development of scaffolds with advanced functionalities and optimized biocompatibility. TiNi alloys have shown promise in improving mechanical properties, as well as providing antimicrobial properties.[28] In addition, there are also reports on the incorporation of Ni^{2+} ions into hydroxyapatite matrices, indicating a positive effect on calcium phosphate formation that favors bone matrix mineralization by enhancing osteointegration and promoting bone tissue recovery.[33,34] In addition, Ni^{2+} can also stimulate blood vessel formation, necessary for bone tissue regeneration.[34] Among Ni-based materials, nickel tungstate ($NiWO_4$) may appear as a good option for improving the bioactivity of chitosan and hydroxyapatite scaffolds. This is because $(WO_4)^{2-}$ provides stability to the material without altering its bioactivity,[35] allowing for the intrinsic production of reactive oxygen species (ROS) and controlled release of Ni^{2+}, in addition to potentially adding antimicrobial properties to the scaffolds.[36–39] Therefore, integrating hydroxyapatite/chitosan/$NiWO_4$ is considered a rational approach for developing advanced structures that combine osteoconductivity with antimicrobial functionality for BTE applications.

To validate this strategy, a systematic characterization route is adopted, encompassing structural, morphological, thermal and mechanical analyses, as well as ion release and biological evaluations. This approach allows direct verification of how composition and scaffold architecture influence bioactivity, stability, and cellular response, ensuring that the desired multifunctional properties are effectively achieved.

2. Materials and methods

2.1. Synthesis of $NiWO_4$

$NiWO_4$ nanoparticles were synthesized using a microwave-assisted hydrothermal method, following the procedure reported by Grasser *et al.*[40] Initially, two separate solutions were prepared: one containing 1×10^{-3} mol of nickel nitrate

($Ni(NO_3)_2{\cdot}6H_2O$, 98%, Sigma-Aldrich) and the other containing 1×10^{-3} mol of sodium tungstate ($Na_2WO_4{\cdot}2H_2O$, 99%, Neon), both dissolved in 50 mL under continuous stirring. After complete dissolution, the nickel solution was added to the tungstate solution, resulting in the formation of a green-colored suspension. The resulting mixture was then transferred to a Teflon-lined reactor and subjected to microwave irradiation (2.45 GHz, 800 W) for 8 min at 160 °C. After the reaction, the precipitate was collected by centrifugation, washed five times with distilled water, and subsequently dried in a conventional oven at 60 °C for 12 h.

2.2. Synthesis of hydroxyapatite

Hydroxyapatite particles were synthesized by chemical precipitation using a peristaltic pump, following the procedure described by Machado *et al.*[41] In this process, the synthesis was carried out *via* chemical precipitation. Initially, 50 mL of an aqueous solution containing 10 mmol of $Ca(NO_3)_2{\cdot}4H_2O$ (99%, Sigma-Aldrich) and 100 mL of a solution containing 6 mmol of $(NH_4)_2HPO_4$ (>98%, Strem Chemicals) were prepared. The pH of both solutions was adjusted to 9.5–10 using NH_4OH (P.A., Synth). After preparation, both solutions were heated to 90 °C. Subsequently, the phosphate solution was added dropwise to the calcium solution at a flow rate of 7 mL min^{-1} using a peristaltic pump. After complete addition of the phosphate solution, the mixture was maintained under continuous stirring and heating for 2 h. At the end of the process, the resulting precipitate was washed eight times with Milli-Q water and three times with ethanol. Finally, the obtained powder was dried in an oven at 60 °C for 24 h.

2.3. Fabrication of chitosan-based composite scaffolds

Chitosan-based scaffolds were fabricated *via* a freeze-drying method. Briefly, 1 g of chitosan (Sigma-Aldrich, medium molecular weight (90–375 kDa), degree of deacetylation: 75–85%) was dissolved in 100 mL of an aqueous 0.5% (v/v) acetic acid solution (Sigma-Aldrich, >99.7%) under magnetic stirring at room temperature for 24 h until complete polymer dissolution. The pH of the resulting solution was subsequently adjusted to 6.0 by dropwise addition of 0.1 M NaOH (Sigma-Aldrich, 97%), monitored using a calibrated pH meter. Pure chitosan scaffolds were obtained by molding the polymer solution into 24-well plates. For the composite scaffolds, hydroxyapatite was incorporated into the chitosan solution at 10% by weight concentration relative to chitosan. Prior to incorporation, all inorganic phases (hydroxyapatite and/or $NiWO_4$) were dispersed in 5 mL of deionized water using a probe-type sonicator operating at 20 kHz and 750 W, applying 50% of the nominal power for 2 min, to reduce viscosity and facilitate homogeneous distribution within the polymeric matrix. After this process, the system was kept under magnetic stirring for 10 minutes to ensure homogeneous particle distribution. For scaffolds without inorganic fillers, an equivalent additional 5 mL of deionized water was added to maintain consistent solid content and processing conditions across all formulations. Scaffolds containing $NiWO_4$ were prepared by adding $NiWO_4$ at concentrations of 2.5, 5, and 10% by weight with respect to chitosan following the same ultrasound procedure.

The scaffolds were named pure chitosan (Ch), chitosan/hydroxyapatite (ChHA), chitosan with nickel tungstate (Ch2.5NiW, Ch5NiW and Ch10NiW) and chitosan/hydroxyapatite/$NiWO_4$ compounds (ChHA2.5NiW, ChHA5NiW and ChHA10NiW). After homogenization, the systems were immersed in liquid N_2 for 15 minutes to induce instantaneous freezing, followed by freeze-drying for 72 h at −70 °C under a vacuum of 0.06 mbar using a TERRONI LS 6000 B freeze-dryer.

2.4. Characterization

X-ray diffraction (XRD) was carried out using a Rigaku diffractometer (model DMax2500PC), at 40 kV, 150 mA using Cu Kα radiation (λ = 1.5406 Å). Scans were recorded within the 2θ range of 10° to 80° with a scan rate of 2° min^{-1}. Fourier transform infrared (FTIR) spectra were recorded in attenuated total reflectance (ATR) mode using a Spectrum Two spectrometer in the spectral range from 400 to 4000 cm^{-1} for identification of functional groups and investigating possible interaction among components. The morphology and microstructure of the scaffolds were viewed by scanning electron microscopy (SEM), and the images were captured using a cold-field emission scanning electron microscope from JEOL, model 7500F. Analysis was carried out in SE mode at an accelerating voltage of 2 kV, an emission current of 10 μA, and a magnification of 50 000×. For isolated inorganic phases, an accelerating voltage of 15 kV was employed to improve image resolution and signal quality. For the energy dispersive spectroscopy (EDS) mapping, the accelerating voltage was adjusted to 15 kV to ensure sufficient elemental excitation. For SEM sample preparation, powder samples were dispersed in deionized water using ultrasonic agitation, and 10 μL of the suspension was drop-cast onto a silicon substrate, dried under ambient conditions, and then analyzed. Scaffold samples were directly mounted onto carbon adhesive tape on aluminum stubs prior to imaging. Transmission electron microscopy (TEM) images were obtained by using a Jeol JEM-2100 F operating at 200 kV. The elemental composition of the scaffolds, with emphasis on calcium and phosphorus, was evaluated by X-ray fluorescence spectrometry (XRF) using a Mini-X2 spectrometer.

Differential Scanning Calorimetry (DSC) was used to assess the thermal behavior, with a calorimeter operating between −50 and 400 °C and an aluminum crucible, with a constant heating/cooling rate of 10 °C min^{-1} and a N_2 flow rate of 0.50 cm^3 min^{-1}, using a DSC204 (Netzsch, Germany). The mechanical properties of the scaffolds were determined by uniaxial compression testing using a universal testing machine (Instron, model 5582) equipped with a 500 N load cell. Tests were performed according to ASTM D1621 (adapted for porous freeze-dried scaffolds) at a crosshead speed of 0.5 mm min^{-1} (n = 10). Cylindrical samples were compressed up to 50% of their original height. The compressive strength was determined from the maximum stress recorded prior to structural collapse of the scaffold. Stress values were calculated by nor-

malizing the applied load to the initial cross-sectional area of each sample.

The stability of the scaffolds in simulated body fluid (SBF) was monitored by measuring pH changes and scaffold mass (n = 3). The scaffolds were placed in 12-well plates containing 5 mL of SBF per well and fully immersed to ensure complete medium absorption throughout the porous structure. The plates were maintained closed and incubated at 37 °C to prevent medium evaporation during the experimental period. After 1, 7, and 14 days of incubation, the scaffolds were removed from the SBF, gently washed with distilled water to remove residual salts, freeze-dried, and weighed to determine mass loss over time. The surface morphology and structural integrity after immersion were further evaluated by SEM analysis at 1, 7, and 14 days. Additionally, after 1, 7, and 14 days of incubation in contact with the fluid, the released analytes were quantified by high-resolution continuous-source molecular absorption spectrometry (HR-CS MAS) using a ContrAA 300 spectrometer (Analytik Jena, n = 3). To determine the porosity, the solvent displacement methodology presented by Sousa *et al.* was used.[42] The scaffolds (n = 3) were initially weighed and then immersed in ethanol for 1 min. To calculate the porosity, the following equation was used:

$$\text{Porosity } (\%) = \frac{(W_w - W_d)100}{\rho(\pi R^2 T)} \quad (1)$$

where W_w is the wet weight of the scaffold, W_d is the dry weight of the scaffold, ρ is the density of the solvent, R is the radius of the scaffold, and T is the thickness of the scaffold.

2.5. *In vitro* assays

2.5.1. Cell culture. *In vitro* assays with MC3T3-E1 pre-osteoblasts and L929 murine fibroblasts, obtained from the Rio de Janeiro Cell Bank (BCRJ), were used to evaluate the biological performance of chitosan-based scaffolds. These assays were conducted under the guidelines of ISO 10993-5:2009. The cells were expanded in culture flasks containing α-MEM (VitroCell) for MC3T3-E1 or DMEM (VitroCell) for L929, both supplemented with 10% fetal bovine serum (FBS, VitroCell) and 1% antibiotic–antimycotic solution. Cell cultures were maintained at 37 °C under a humidified atmosphere with 5% CO_2, kept subconfluent, and subcultured weekly until use in the experiments.

2.5.2. Preparation of materials for indirect contact tests. Prior to the biological assay, the scaffolds were sterilized by exposure to ultraviolet radiation under aseptic conditions for 24 h. Biocompatibility assessment followed the guidelines of ISO 10993, conducted using two distinct approaches: direct and indirect contact.[43] In the direct contact method, cells were seeded in immediate contact with the surface of the sterilized scaffolds. For the indirect contact method, an extract (conditioned medium) was prepared using a mass/volume ratio of 0.1 g mL^{-1}. The scaffolds were immersed in culture medium (DMEM or α-MEM, depending on the cell line) supplemented with 10% FBS and incubated at 37 °C under a humidified atmosphere with 5% CO_2 for 24 h. After this period, the extract was filtered through a 0.22 μm membrane to ensure the removal of any debris before cell testing.

2.5.3. Metabolic activity. The MC3T3-E1 pre-osteoblast and L929 murine fibroblast cell lines were subjected to metabolic activity assays following distinct protocols for direct and indirect tests. In both cases, the cells were initially seeded in 48-well plates at a density of 1×10^4 cells per well. In the indirect test, the cells were kept in culture for 24 h to allow for complete adhesion. After this period, the original culture medium was removed and replaced with 500 μL of conditioned medium. For the direct test, the scaffolds were previously positioned in the wells and immersed in 500 μL of complete culture medium for 4 h, ensuring total absorption of the medium by the porous structure and hydrolytic equilibrium of the material. Only after this interval were the cells seeded directly onto the surface of the scaffolds. Metabolic activity was monitored by the resazurin assay at 1, 3, and 7 days for L929 cells (direct method) and 1, 7, and 14 days for MC3T3-E1 cells (direct and indirect methods). At each time point, the medium was replaced with 200 μL of resazurin solution (70 μM), with incubation for 4 h at 37 °C. Fluorescence was measured using a GloMax microplate reader (Promega, excitation at 520 nm and emission between 580 and 640 nm), with results expressed as a percentage relative to the control without any treatment. All experiments were performed in triplicate across three independent assays (n = 9).

2.5.4. Intracellular ROS. Intracellular generation of ROS was evaluated using the fluorescent probe 2′,7′-dichlorodihydrofluorescein diacetate (DCFH-DA, Sigma-Aldrich). MC3T3-E1 pre-osteoblasts were seeded in 48-well black plates under the same experimental conditions described, using indirect contact. After 24 h of adhesion, the treatments were applied. On days 1, 7, and 14 of exposure, the cells were washed twice with phosphate-buffered saline (PBS), and then 200 μL of a 100 μM DCFH-DA solution prepared in PBS was added. Incubation of the plates was carried out for 30 min at 37 °C under a humidified atmosphere, containing 5% CO_2, protected from light. The probe solution was then removed and the wells were washed with PBS, after which 100 μL of phosphate-buffered saline (PBS, Vitrocell) was added. Fluorescence intensity was read using a BioTek microplate fluorometer (Promega) set to excitation and emission wavelengths of 485 and 530 nm, respectively. All experiments were performed in triplicate across three independent assays (n = 9).

2.5.5. Nitric oxide analysis. The production of reactive nitrogen species (RNS) was quantified using the Griess assay, which measures nitric oxide levels by forming nitric oxide (NO). MC3T3-E1 pre-osteoblasts were seeded in 48-well flat-bottom plates under the same experimental conditions described previously, using indirect contact. After 24 h of adhesion, the treatments were applied. On days 1, 7, and 14 of exposure, 50 μL of the culture supernatant was transferred to a new microplate, followed by the addition of 50 μL of freshly prepared Griess reagent. The reagent consisted of a 1 : 1 mixture of Solution A (1% sulfanilamide (Synth; 99%) in

phosphoric acid (Sigma-Aldrich; 85%)) and Solution B (0.1% *N*-(1-naphthyl)ethylenediamine dihydrochloride (Sigma-Aldrich, 98%)). The mixture was incubated at room temperature in the dark for 15 min. Absorbance was measured at 540 nm using a BioTek microplate spectrophotometer (Promega). Nitric oxide concentrations were calculated from a deficiency curve constructed with standard nitrite solutions (nM), according to the modified Griess reagent protocol (Sigma-Aldrich, G4410). All experiments were performed in triplicate across three independent assays ($n = 9$).

2.5.6. Extracellular matrix mineralization. For the mineralization assays, MC3T3-E1 osteoblastic cells were seeded in 12-well plates (Corning Incorporated) at a density of 1×10^5 cells per well. After a 24 h period under standard culture conditions for cell adhesion stabilization, the basal medium was replaced with the respective conditioned media. The formation of the mineralized matrix was evaluated after 7 and 14 days of incubation using Alizarin Red S (ARS, Sigma-Aldrich; pH 4.2) staining. At each experimental point, the cultures were gently washed with PBS and fixed in 4% paraformaldehyde (PFA, Synth) for 15 min. After triple washing with distilled water, the wells were incubated with 2% (w/v) ARS solution for 15 min, followed by further washes to remove excess dye. For the quantification step, the dye complexed with the mineral deposits was solubilized in a 10% (w/v) cetylpyridinium chloride solution (Synth) under stirring for 1 h. The absorbance of the resulting solution was measured at 570 nm using a microplate spectrophotometer (BioTek Instruments, Promega). As a negative control, only the basal medium was used, while the positive control consisted of osteogenic medium (α-MEM supplemented with 10% FBS, 1% β-glycerophosphate, 1% L-ascorbic acid 2-phosphate, and 0.1% dexamethasone). All experiments were performed in triplicate across three independent assays ($n = 9$).

The Ca^{2+} and Ni^{2+} measurements in samples were performed using a high-resolution molecular absorption spectrometer (HR-CS MAS ContrAA model 300, Analytik Jena, Jena, Germany). The linear range (LR), limit of detection (LOD), limit of quantification (LOQ), and linear adjustment coefficient (r^2) were LR = 0.0025 to 0.075 mmol L^{-1}, LOD = 0.0027 mmol L^{-1}, LOQ = 0.009 mmol L^{-1}, and $r^2 = 0.998$ for Ca^{2+}. For Ni^{2+}, LR = 0.0017 to 0.051 mmol L^{-1}, LOD = 0.001 mmol L^{-1}, LOQ = 0.003 mmol L^{-1}, and $r^2 = 0.999$.

2.5.7. Wound healing (scratch assay). MC3T3-E1 cells were seeded in 12-well plates at a density of 1×10^5 cells per well and incubated for 24 h to allow adhesion. A linear scratch was created in the confluent monolayer using a sterile 200 μL pipette tip, and detached cells were removed by washing with PBS. Conditioned medium containing the treatment and 1% of FBS at predefined concentrations was then added (1 mL), and the cells were incubated for up to 48 h. Images of the wound area were acquired at 0, 24, and 48 h. Wound closure was quantified using ImageJ software by measuring the reduction in wound area over time and was calculated according to eqn (2):

$$\text{Wound closure } (\%) = \frac{A_0 - A_t}{A_0} \times 100 \quad (2)$$

where A_0 and A_t correspond to areas at 0 h and at time t, respectively. All experiments were performed in triplicate ($n = 3$).

2.5.8. Cell adhesion. MC3T3-E1 cells were seeded directly onto the scaffold surface using a density of 1×10^5 cells per scaffold. Prior to this step, the scaffolds underwent a pre-wetting process in complete culture medium for 4 h to achieve hydrolytic equilibrium of the matrix. After seeding, the samples were maintained under standard culture conditions for 24 h to allow for cell adhesion stabilization. Cell morphology and distribution were evaluated by confocal laser scanning microscopy (SP8 AOBS Tandem Scanner System, Leica Microsystems) using specific fluorescence labeling. For image preparation, the scaffolds were gently washed with PBS to remove non-adherent cells and fixed in 4% paraformaldehyde (PFA; Synth). The actin cytoskeleton was visualized using phalloidin staining conjugated to Alexa Fluor 488 (Invitrogen), while the nuclei were contrasted with 4′,6-diamidino-2-phenylindole (DAPI; Invitrogen). The resulting images allowed for detailed analysis of cell–material interaction and cytoskeletal organization on the porous structures.

2.5.9. Antibacterial assay (CFU counting method). The antibacterial efficacy of the materials was tested against *Escherichia coli* (ATCC 25922) and *S. aureus* (ATCC 29213) strains.[44] The microorganisms were cultured until they reached specific optical densities corresponding to inocula of approximately 1×10^8 CFU mL^{-1}. Following the *in vitro* tests, the scaffolds were inoculated at a concentration of 0.1 g mL^{-1} for 24 h at 37 °C in Muller Hilton (MH) broth. As a control, the bacterial suspension without exposure to the materials was used. After the incubation time, the tubes were homogenized for 1 minute and subjected to serial dilutions. The quantification of colony-forming units (CFUs) was performed by seeding 10 μL of each dilution onto Petri dishes containing MH agar. The plates were incubated at 37 °C for 24 h. The final CFU mL^{-1} count was compared to the control group to determine the inhibition rate. The experiment was conducted in three independent trials ($n = 3$) to ensure the reproducibility of the results.

2.5.10. Statistical analysis. The statistical treatment of the data was performed using GraphPad Prism software (version 7.0). Initially, the data distribution was evaluated using descriptive statistics and frequency histograms, with normality verified by the Shapiro–Wilk test. For parametric data, the results were expressed as mean ± standard deviation. Variations between experimental groups were analyzed *via* one-way analysis of variance (ANOVA), followed by Dunnett's *post-hoc* test to identify significant differences in relation to the control group. In all analyses, a significance level of <0.05 was adopted.

3. Results and discussion

3.1. Characterization

First, the structural properties and morphological characteristics of $NiWO_4$ nanoparticles and hydroxyapatite obtained by

XRD, FTIR and SEM were investigated (Fig. S1). The diffraction pattern of powdered $NiWO_4$ does not display the typical set of reflections associated with a well-ordered monoclinic structure. Instead, broad and low-intensity peaks are observed, indicating limited long-range crystalline order. These results indicate that the $NiWO_4$ obtained in this work can be described as a structurally disordered system, in which distorted [NiO_6] and [WO_6] octahedral units are irregularly arranged within the crystal lattice. This behavior is consistent with a partially disordered framework previously reported in the literature, resulting in a semicrystalline material.[40] In contrast, hydroxyapatite exhibits well-defined and high-intensity diffraction peaks, characteristic of a highly crystalline material. The observed peaks correspond to the reference pattern characteristic of an anorthic crystal system, space group $P\ 63/m$, confirming the formation of the expected crystalline phase and the material's high level of structural organization.[45] In FTIR analysis, $NiWO_4$ displays characteristic metal–oxygen vibrational modes, with bands associated with the stretching of W–O bonds in $(WO_4)^{2-}$ units and Ni–O bonds, consistent with tungstate-based materials reported in the literature.[46] Hydroxyapatite exhibits well-defined phosphate-related stretching bands, with absorptions at approximately 1031 cm^{-1} and 989 cm^{-1}, assigned to asymmetric and symmetric P–O stretching modes, respectively, and bands at 636 cm^{-1} and 557 cm^{-1}, corresponding to O–P–O bending vibrations.[47] The morphology of the materials obtained was consistent with previously published work.[24,39] $NiWO_4$ has an irregular polyhedral morphology, with an average size of 20.8 ± 7.6, while hydroxyapatite has a nanorod morphology with an average size of 267.2 ± 92.6 nm.

Once the components were analyzed, their interaction with chitosan for the formation of scaffolds *via* freeze drying was evaluated. Fig. 1A shows the diffractograms obtained for the scaffolds with different concentrations of $NiWO_4$ and hydroxyapatite. Pure chitosan (Ch sample) presents diffraction peaks centered at 16.4° and 25.1°, corresponding to its semicrystalline anhydrous form. This structural profile results from the dissolution process in acetic acid followed by drying at low temperatures, which promotes a partial organization of the polymer chains in the polysaccharide matrix.[48,49] This behavior can be attributed to the prior adjustment of the pH to values near 6, under which partial protonation of the chitosan amino groups occurs, reducing electrostatic repulsion between polymer chains and favoring intermolecular interactions, such as hydrogen bonding.[50–52] Some well-defined peaks can also be observed, related to the formation of sodium acetate due to pH regulation, corroborating the findings of the previous study by Assis *et al.*[14] Regarding the composite materials, it is possible to observe that all samples maintain the initial characteristics observed for chitosan. Furthermore, no well-defined diffraction peaks attributable to $NiWO_4$ or hydroxyapatite are observed at lower loadings. This behavior can also be explained by the highly porous architecture of the chitosan scaffold. The porous network likely promotes partial encapsulation of the nanoparticles within the polymeric matrix, which may further diminish their effective crystalline contribution, making the detection of distinct diffraction peaks more difficult. However, for samples containing higher amounts of $NiWO_4$, a broad amorphous halo becomes visible in the 15–40° (2θ) range, which can be associated with the incorporation of $NiWO_4$ into the composite and may serve as indirect evidence of its presence. In the case of hydroxyapatite, no clear diffraction peaks are identified because its main reflection overlaps with a strong diffraction peak from sodium acetate present in the system, which masks its characteristic signal.

The FTIR spectra of scaffolds are shown in Fig. 1B. Chitosan shows characteristic absorption bands associated with its polymeric structure. The band located at 1016 cm^{-1} is related to C–O deformation vibrations. The band at 1545 cm^{-1} is attributed to N–H bending vibrations, indicating the presence of N-acetylated units in the chitosan backbone.[53] The band observed at 1405 cm^{-1} is associated with polymer chain bending, specifically corresponding to C–H bending vibrations. The peak at 1153 cm^{-1} was assigned to the asymmetric stretching of the glycosidic bridge (C–O–C), whereas the bands at 1047 cm^{-1} and 1016 cm^{-1} are consistent with skeletal vibrations involving C–O stretching, which are characteristic of the chitosan matrix.[54] In the composite scaffolds, the FTIR spectra maintain the characteristic vibrations of chitosan,

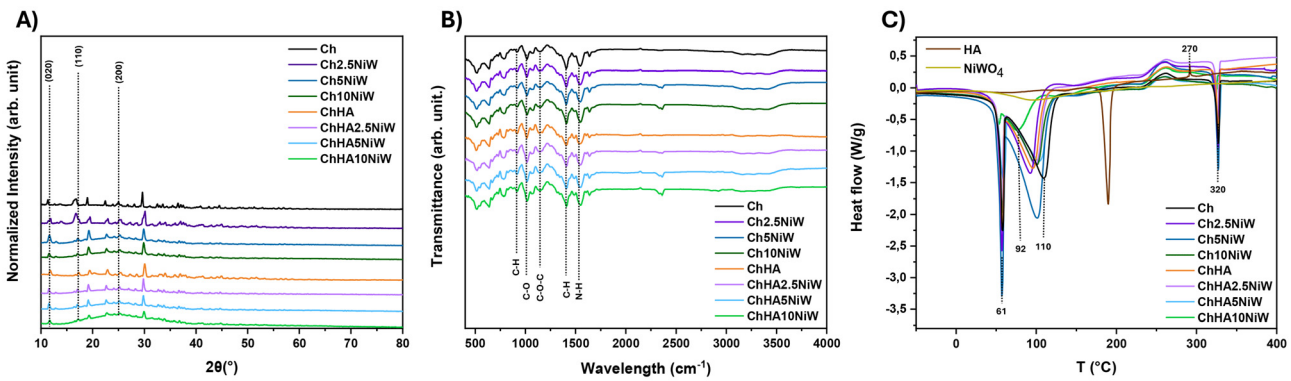

Fig. 1 Structural and thermal characteristics of the scaffold composites: (A) XRD patterns, (B) FTIR spectra, and (C) DSC analysis.

without the appearance of new bands or significant shifts, indicating that the incorporation of the inorganic phases into the polymeric scaffold occurs without altering their fundamental chemical structures, consistent with the XRD analysis.

DSC analysis was performed not only to verify the thermal behavior of the scaffolds, but also to evaluate how the addition of $NiWO_4$ and hydroxyapatite alters the mobility of chitosan polymer chains (Fig. 1C). Specifically, endothermic peaks were observed at approximately 61, 110, and 320 °C, in addition to an exothermic peak at 270 °C.[55] The peaks at 61, 270, and 320 °C are related to the relaxation of the amorphous regions in the polymer structure, chitosan depolymerization, and degradation of the chitosan backbone, and are not altered by the addition of inorganic fillers. However, the peak at approximately 110 °C, related to dehydration processes or the release of residual water molecules, is shifted to lower temperatures, reaching values as low as 92 °C upon the incorporation of $NiWO_4$. This shift may be attributed to modifications in the polymeric network induced by the presence of the inorganic phase. The incorporation of nanoparticles can alter intermolecular interactions within the matrix, modify heat distribution, and influence polymer chain mobility, thereby reducing the energy required for water release.[14] A similar behavior was reported by Ghaziof *et al.*, who observed a decrease in the dehydration temperature of polymer nanocomposites after the incorporation of Au nanoparticles.[56] In that study, the nanoparticles worked as plasticizers, making the polymer free volume and segmental mobility higher. This led to lower dehydration temperatures. These results corroborate the hypothesis that inorganic nanoparticles can affect the thermal behavior of the composite by altering its microstructural arrangement and intermolecular interactions.

The morphology of the scaffolds was investigated by SEM and is shown in Fig. 2. For the chitosan obtained by freeze drying, the formation of lamellar macrostructures with large pores is observed.[57] The average pore size obtained was 0.065 ± 0.004 mm and the lamellae thickness was 0.072 ± 0.008 mm. This morphology is consistent with the work of Zhang *et al.*,[58] who obtained chitosan scaffolds from freeze drying. Upon adding inorganic fillers, some changes can be observed. The lamellae become more organized with the addition of hydroxyapatite, obtaining pores with an average size of 0.052 ± 0.005 mm and a lamellar thickness of 0.167 ± 0.047 mm. Upon adding $NiWO_4$ with or without hydroxyapatite, the more organized lamellar structure begins to collapse, forming the biggest pores with interconnections between the lamellae. For samples Ch2.5NiW, Ch5NiW, and Ch10NiW, the obtained pore sizes were 0.062 ± 0.006 mm, 0.071 ± 0.004 mm, and 0.079 ± 0.005 mm while the lamellar thicknesses were 0.100 ± 0.124 mm, 0.132 ± 0.011 mm and 0.209 ± 0.026 mm, respectively. For samples ChHA2.5NiW, ChHA5NiW, and ChHA10NiW, the obtained pore sizes were 0.078 ± 0.008 mm, 0.098 ± 0.009 mm, and 0.039 ± 0.005 mm, while the lamellar thicknesses were 0.148 ± 0.013 mm, 0.182 ± 0.012 mm, and 0.185 ± 0.008 mm. This factor may be directly associated with the interaction of water molecules with the composite, which is altered due to the addition of inorganic fillers, as evidenced by the DSC results. Navas *et al.*[59] manufactured chitosan scaffolds with polyvinyl alcohol (PVA) and SiO_2 nanoparticles using the freeze-drying method and observed similar behavior, associating the modification of this structure with strong hydrogen bonding interactions between the hydroxyl groups of PVA and the primary amino groups of chitosan with the surface of SiO_2, improving the distribution, size and number of pores. The morphology of the scaffolds with well-defined, interconnected pores and lamellar structures facilitate nutrient and metabolite transport, oxygen diffusion, cell adhesion, proliferation, and migration, which are essential for proper biological performance.[60,61]

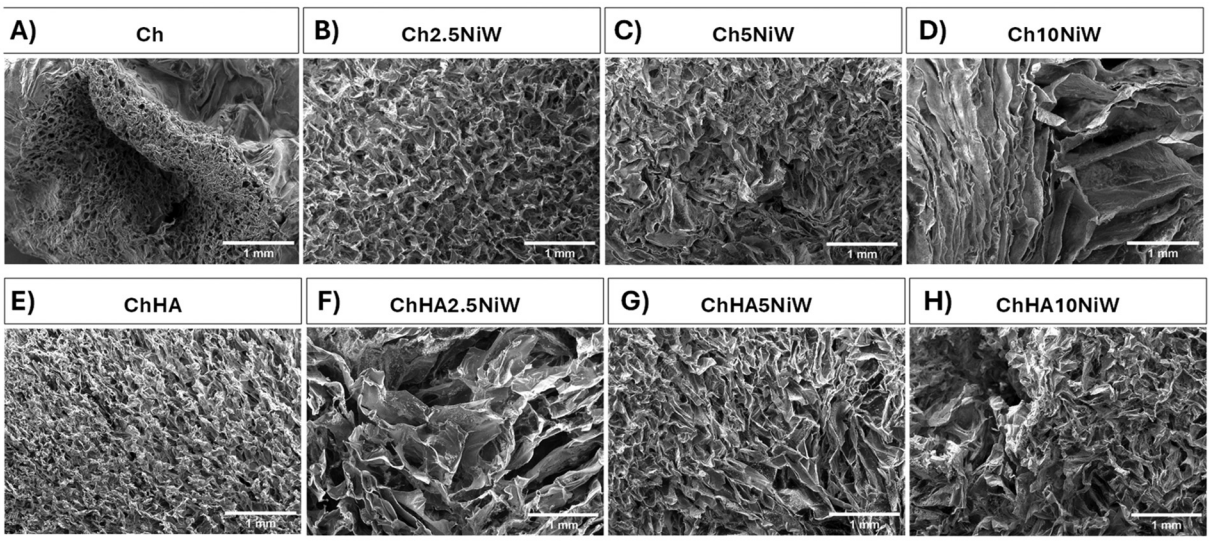

Fig. 2 Morphological analysis of scaffolds by SEM: (A) Ch, (B) Ch2.5NiW, (C) Ch5NiW, (D) Ch10NiW, (E) ChHA, (F) ChHA2.5NiW, (G) ChHA5NiW, and (H) ChHA10NiW.

The porosity results (Fig. S2) showed that the composition of the scaffolds directly influences the structural architecture. The pure chitosan sample presented intermediate porosity (~40%), a typical characteristic of freeze-drying structures.[62] This result is consistent with the SEM observations, which showed lamellar macrostructures with relatively large pores generated during ice crystal growth and sublimation. The incorporation of hydroxyapatite resulted in a significant reduction in porosity (~15%), which can be attributed to the greater packing of the matrix and the possible partial filling of the pores by the inorganic phase, promoting a denser and more organized structure.[63] This behavior agrees with the SEM images, where the addition of hydroxyapatite led to a more organized lamellar arrangement and smaller pore sizes, indicating a more compact structural organization of the scaffold. On the other hand, the addition of $NiWO_4$ promoted a progressive increase in porosity in all samples present, reaching values greater than 55% at the highest concentration. This increase in porosity correlates with the morphological changes observed in SEM, where the lamellar organization became less defined and larger interconnected pores were formed. This behavior is associated with the modification of the pore formation process during freezing, since the presence of the semiconductor can alter the intermolecular interactions and the dynamics of ice crystal formation, resulting in larger pores and interconnected lamellae, as also evidenced by the increase in pore size measured from the SEM images. Such effects become more pronounced at higher $NiWO_4$ contents, where the structural reorganization of the lamellae leads to a more open and interconnected porous network. Santos *et al.* demonstrated this behavior by adding grape seed oil (GSO) to a chitosan scaffold, in which the porosity of the scaffolds increased by about 17%, with the increase being more visible in samples with higher concentrations.[64]

As previously observed, it is not possible to detect the addition of inorganic fillers using XRD or FTIR, with the initial effects of their addition being observed in DSC and SEM analyses. Fig. 3 shows the EDS mappings of the scaffolds to confirm the addition of $NiWO_4$ and hydroxyapatite, while Table S1 presents the semi-quantitative elemental composition obtained from EDS analysis. For the Ch sample, it is observed that the scaffolds are formed primarily by C, O, and a small amount of N, as expected due to the polymer composition. For the ChHA sample, the appearance of Ca and P, the base elements of hydroxyapatite, is observed. For the ChNiW samples, Ni and W are visible at all concentrations. W is more evident due to its atomic weight and the accelerating voltage used (15 kV), which does not provide sufficient energy to optimally excite the Kα lines of Ni (7.47 keV). For the ChHANiW samples at all concentrations, it is possible to observe C, O, and N from chitosan, Ca and P from hydroxyapatite, and Ni and W from $NiWO_4$. Additionally, Table S1 presents the elemental composition in wt% obtained from EDS analysis, showing values that are consistent with the nominal compositions used during scaffold preparation. The metal content determined by EDS is comparable to the values obtained by XRF analysis (Table S2). This analysis shows that the incorporation of all components was successfully achieved.

The stability of scaffolds is essential for maintaining their support function and bioactivity. Therefore, their stability in solution was analyzed over 14 days, along with changes in the pH of the medium (Fig. 4). Water uptake is governed by both accessible porosity (connectivity/pore size distribution) and the hydrophilicity of the solid phase. All materials exhibited

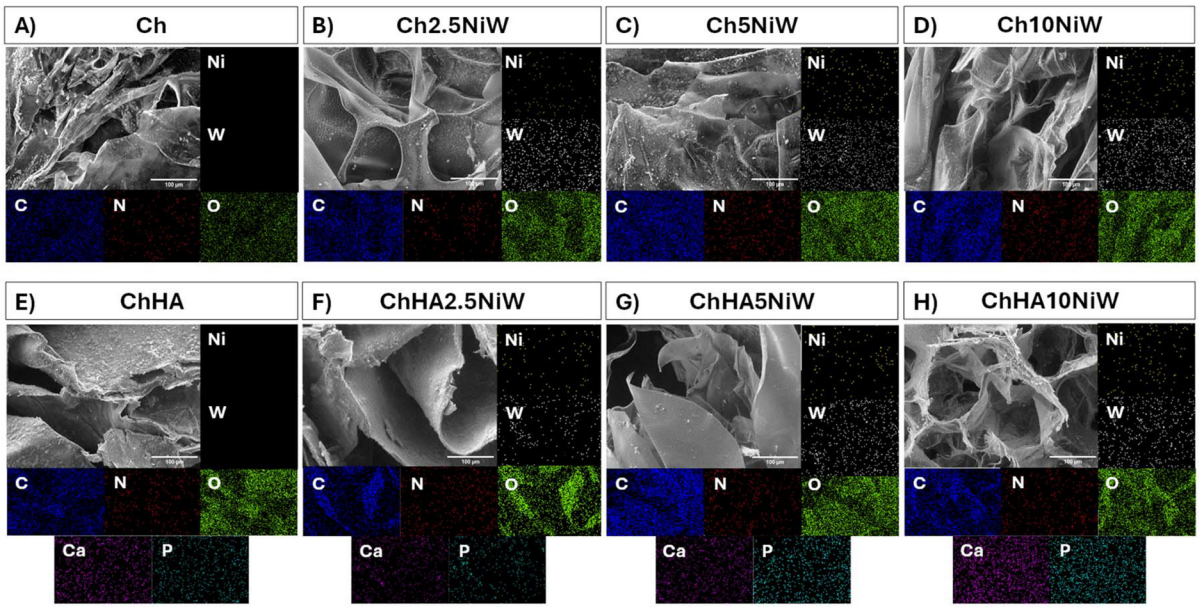

Fig. 3 EDS mapping of the scaffolds: (A) Ch, (B) Ch2.5NiW, (C) Ch5NiW, (D) Ch10NiW, (E) ChHA, (F) ChHA2.5NiW, (G) ChHA5NiW, and (H) ChHA10NiW.

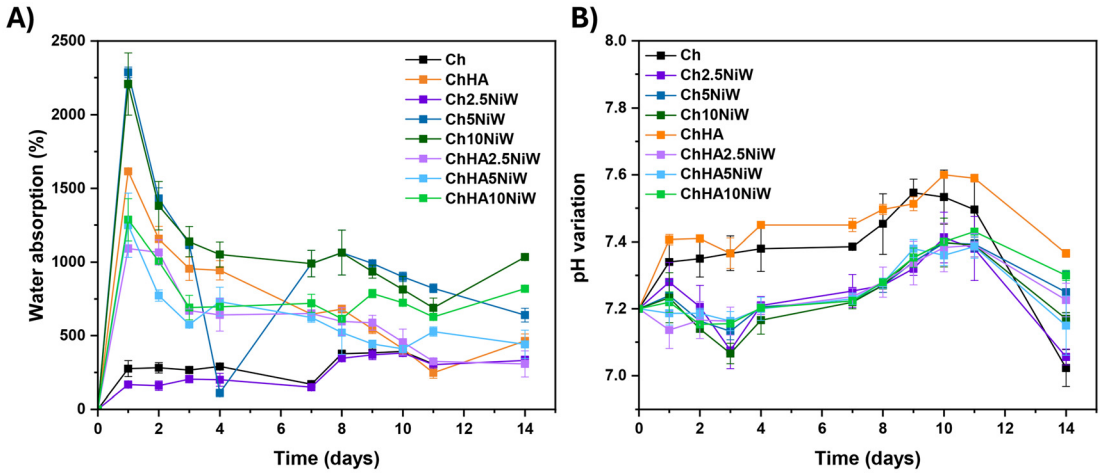

Fig. 4 Behavior of scaffolds in solution (SBF) at 37 °C for 14 days: (A) mass variation and (B) pH variation. Results are presented as mean ± standard deviation (n = 10).

high water uptake during the first two days, indicating rapid penetration of the solution into the porous structure, which is an expected behavior for chitosan-based scaffolds due to their high pore interconnectivity. Pure chitosan scaffolds showed lower absorption values, which is consistent with their intermediate porosity (~40%) and relatively organized lamellar morphology observed by SEM. The incorporation of hydroxyapatite significantly increased water absorption, despite the reduction in overall porosity, which can be attributed to its hydrophilic nature and to the formation of polymer–ceramic interfaces that enhance capillary-driven water retention. Although hydroxyapatite reduces the total porosity by partially occupying pore space, it increases the affinity of the scaffold for aqueous media, facilitating water retention within the structure. Over time, the absorption values decreased and stabilized, indicating that the material preserved its structural integrity after the initial swelling without network collapse. This behavior is also consistent with the SEM observations showing more organized lamellae and smaller pores in the HA-containing scaffolds, which contribute to structural stability during swelling.

Scaffolds containing $NiWO_4$ exhibited strongly concentration-dependent behavior. At low $NiWO_4$ contents, a moderate and stable water absorption profile was observed, which agrees with the moderate increase in porosity and the preservation of the lamellar architecture observed by SEM. In contrast, higher $NiWO_4$ concentrations (Ch5NiW and Ch10NiW) led to extremely high water uptake during the first few days, followed by pronounced fluctuations over time, indicating initial dimensional instability. This behavior correlates with the increase in porosity and the partial disruption of the lamellar structure identified in the SEM images, which results in a more open and heterogeneous pore network that facilitates rapid solution penetration but may also promote local structural rearrangements after swelling. Notably, scaffolds containing both hydroxyapatite and $NiWO_4$ exhibited more stable absorption profiles over time, particularly at intermediate concentrations. Among these systems, the ChHA2.5NiW scaffold displayed the most balanced behavior, combining relatively high-water uptake with minimal fluctuations throughout the evaluation period. This behavior suggests that hydroxyapatite partially stabilizes the porous architecture while $NiWO_4$ contributes to increasing the accessible pore volume, resulting in a structure that favors solution penetration while maintaining morphological integrity. Morphological analysis further supports this interpretation, as ChHA2.5NiW presents well-defined and interconnected pores, more continuous lamellae, and a reduced presence of collapsed regions or particle agglomerates. This behavior was also observed by Correia *et al.*[65] in composite systems containing chitosan and bioactive glass nanoparticles (BG-NPs), whose swelling results indicated a greater solvent absorption capacity compared to pure chitosan. This behavior was attributed to the hydrophilic nature of the BG nanoparticle fraction, which intensifies the interaction of the material with the solvent.

The mass variation of the scaffolds after 1, 7, and 14 days of immersion in SBF (Fig. S3) was determined after lyophilization, reflecting the net changes occurring at the scaffold surface during the immersion period. In general, the variations observed were moderate, suggesting that no abrupt degradation or extensive mineral deposition by chemical segregation occurred during the evaluated period. After 1 day, the relatively small mass variations indicate the initial interaction between the scaffold surface and the ionic environment of SBF, which may involve the adsorption of ions and the early stages of surface reorganization. These initial changes are consistent with the porous architecture observed by SEM, which facilitates rapid contact between the scaffold surface and the surrounding solution. On day 7, some samples exhibited a slight increase in mass, particularly those containing inorganic phases. This behavior may be associated with the progressive deposition of calcium phosphate species on the

scaffold surface, which is commonly observed in bioactive polymer–inorganic composites. In addition, the higher porosity and interconnected lamellar structure identified in SEM can favor ionic diffusion within the scaffold, increasing the effective surface area available for these interactions. After 14 days, the mass variation of most samples slightly decreased or stabilized. This trend suggests that the system approaches a relatively stable condition in which surface deposition and slow matrix reorganization occur simultaneously, without significant structural loss. Such behavior is typical of porous chitosan-based scaffolds immersed in SBF, where surface interactions occur progressively without drastic mass changes over short immersion periods. After 14 days in SBF, images were obtained to analyze the scaffold structure (Fig. S4). The images showed clear changes in the porous structure, such as parts of it collapsing and the pore walls getting thicker, as well as less uniformity in the structure. These observations indicate matrix relaxation and the initiation of hydrolytic degradation, while the overall 3D structure remained preserved.

The chemical stability of the scaffolds was assessed by monitoring the pH variation of the solution in direct contact with the materials, allowing the evaluation of ion release and possible matrix degradation. Overall, all scaffolds maintained pH values close to neutrality (~7.0–7.6), indicating good chemical stability and compatibility with physiological environments, without abrupt degradation or significant acidification/alkalinization of the medium. Pure chitosan scaffolds exhibited a gradual increase in pH during the initial days and between days 7 and 10, followed by a slight decrease at the end of the experiment. This behavior can be attributed to the protonation and deprotonation processes of amine groups and to the establishment of an acid–base equilibrium between the polymeric matrix and the surrounding medium. Hydroxyapatite-containing scaffolds presented slightly higher pH values, associated with the mildly basic nature of HA and the controlled release of Ca^{2+} ions, whose concentration increased over time. Despite the higher water absorption, the pH remained stable, indicating chemical robustness.

For $NiWO_4$-containing scaffolds, pH values remained close to neutrality with only minor oscillations. The lowest concentration (Ch2.5NiW) exhibited the most stable pH profile, which is associated with lower ion release and good chemical compatibility between the inorganic phase and the polymer matrix. At higher $NiWO_4$ contents, a slight decrease in pH was observed during the first few days, consistent with increased ion release; however, equilibrium was rapidly achieved, indicating the absence of progressive chemical degradation. Finally, scaffolds combining hydroxyapatite and $NiWO_4$ presented intermediate and more uniform pH values over time, reinforcing the buffering role of hydroxyapatite. In particular, the ChHA2.5 scaffold exhibited the most stable physicochemical behavior, supporting high hydration levels while maintaining dimensional and chemical stability. Overall, these results demonstrate that scaffold stability is strongly governed by internal architecture and network homogeneity. Scaffolds with more organized structures and reinforced pore walls, especially those containing hydroxyapatite and intermediate $NiWO_4$ concentrations, can sustain prolonged exposure to aqueous environments, confirming their suitability for tissue engineering applications.

Analyzing the levels of Ca^{2+} and Ni^{2+} is fundamental for monitoring, respectively, the mineralization potential of the matrix and the balance between stimulating bioactivity and maintaining the toxicological safety of the scaffold. The results of the ion release are shown in Table 1. The W^{6+} results were not included because they were below the detection limit of the equipment. A gradual decrease in Ca^{2+} concentration over time was observed for hydroxyapatite-based scaffolds, indicating consumption of Ca^{2+} ions from the SBF, which is generally associated with the nucleation and growth of an apatite layer on scaffolds.[66] Garbo *et al.*[67] observed similar behavior in advanced hydroxyapatites with Mg^{2+} substitutions in SBF. For the ChNiW samples at all concentrations, the values did not exceed 0.012 mM after 14 days, even for the highest $NiWO_4$ concentration (10%). As shown in Table 1, Ni^{2+} release increases with both $NiWO_4$ content and immersion time, confirming dose-dependent and time-dependent behavior. Importantly, the released concentrations remain in the millimolar-to-submillimolar range, indicating a controlled and gradual release profile rather than an abrupt ion burst. These values do not reach levels considered toxic for standard L929 fibroblast cell lines, where the TC_{50} values obtained are 0.1–0.4 mM.[28,68] For the ChHANiW scaffolds, the release of Ca^{2+} is like that of the ChHA scaffolds, indicating that $NiWO_4$ does not interfere with the mineralization of the apatite layer. The Ni^{2+} release behavior is similar for the ChHANiW samples with 2.5 and 5% $NiWO_4$, but for the 10% loading, a more pro-

Table 1 Ion release (mM) results obtained for the scaffolds on days 1, 7, and 14

Sample	Days	Ca^{2+} [a] (mM)	Ni^{2+} (mM)
ChHA	1	3.400	—
	7	2.220	—
	14	2.090	—
Ch2.5NiW	1	—	0.003
	7	—	0.006
	14	—	0.009
Ch5NiW	1	—	0.003
	7	—	0.006
	14	—	0.008
Ch10NiW	1	—	0.005
	7	—	0.012
	14	—	0.012
ChHA2.5NiW	1	3.990	0.002
	7	3.070	0.007
	14	3.010	0.004
ChHA5NiW	1	3.230	0.003
	7	3.000	0.006
	14	2.550	0.007
ChHA10NiW	1	3.810	0.010
	7	3.300	0.013
	14	2.510	0.036

[a] For Ca^{2+} analysis, the samples were diluted in ultrapure water, and the concentration was adjusted using the dilution factor.

nounced increase is observed, particularly at day 14, reaching 0.036 mM. This value is still below TC_{50}; however, it is approximately three times higher than that observed for the corresponding scaffold without hydroxyapatite, possibly indicating a modification in ion release dynamics associated with the composite microstructure rather than a direct cytotoxic risk.

Mechanical support is fundamental in BTE because the scaffold must mimic the structural integrity of native bone, ensuring mechanical stability for cell adhesion and resisting physiological stresses throughout the regeneration process and the formation of a new mineralized matrix. The mechanical behavior of chitosan-based scaffolds is strongly influenced by the morphological changes induced by the incorporation of hydroxyapatite and $NiWO_4$ particles (Table 2). The pure chitosan scaffold presents a more compact structure with thinner lamellae, forming a more continuous and homogeneous matrix, which favors greater initial stiffness, reflected by higher values of elastic modulus (E). With the addition of hydroxyapatite and the increase in $NiWO_4$ content, a progressive transition to a more open and porous architecture is observed, with thicker lamellae, which favors greater matrix flexibility and greater water retention by the scaffolds, as observed by DSC. This increase in porosity and the discontinuity of the polymer network result in a significant reduction in E. On the other hand, the presence of well-distributed inorganic phases in moderate amounts, especially for the samples Ch5NiW and ChHA5NiW, contributes to the reinforcement of the scaffold walls and structures, increasing their resistance to collapse under compressive loading and, consequently, increasing the maximum compressive stress (σ_u). At higher $NiWO_4$ contents, the excessive incorporation of particles can promote structural heterogeneity and the formation of defects, such as agglomerates and weakened interfacial regions, which act as stress concentrators and compromise load-bearing efficiency. Taken together, the results indicate that the mechanical performance of the scaffolds stems from the balance between the greater conformability associated with porosity and the localized reinforcement of the structural walls, with an optimal content of the inorganic phase observed to maximize compressive strength. Li *et al.*[69] observed that freeze-dried chitosan/hydroxyapatite scaffolds reached optimal compressive performance at moderate HA contents, while excessive ceramic loading led to reduced modulus and strength and premature densification under compression. In contrast, Abdian *et al.* reported a progressive increase in the compressive strength of the scaffolds with increasing ceramic content.[70]

Table 2 Mechanical properties of the composite scaffolds. Results are presented as mean ± standard deviation (n = 10)

Sample	Elastic modulus (E, kPa)	Maximum compressive stress (σ_u, kPa)
Ch	144.28 ± 47.09	464.80 ± 105.08
ChHA	19.66 ± 2.54	627.76 ± 94.60
Ch2.5NiW	21.10 ± 7.67	617.82 ± 106.89
Ch5NiW	61.45 ± 4.16	678.77 ± 238.50
Ch10NiW	17.35 ± 2.41	502.51 ± 152.81
ChHA2.5NiW	9.13 ± 4.47	593.81 ± 138.75
ChHA5NiW	24.66 ± 8.76	815.10 ± 136.32
ChHA10NiW	13.84 ± 0.93	526.71 ± 75.95

3.2. *In vitro* assays

Once the structural, morphological, and mechanical properties, as well as the stability of the scaffolds, were analyzed, *in vitro* tests were conducted to assess the potential use of these scaffolds in BTE, seeking to correlate their biological performance with their physicochemical properties. The metabolic activity of MC3T3-E1 cells was evaluated by the resazurin assay under direct and indirect contact conditions. The combination of these approaches is fundamental to distinguishing the biological effects resulting from the immediate cell interaction with the scaffold surface from those caused by byproducts or ions released by the material into the culture medium. The results of metabolic activity were analyzed in both cases at 1, 7, and 14 days (Fig. 5), and according to ISO 10993, values below 70% are considered toxic.

For direct contact (Fig. 5A) on day 1, a slight statistically significant increase in the metabolic activity of MC3T3-E1 cells was observed for the Ch and ChHANiW scaffolds at all concentrations (2.5, 5, and 10%). The other samples did not show statistically significant changes in metabolic activity compared to the control. On day 7, a slight reduction in metabolic activity to values close to 85% was observed for the Ch2.5NiW, Ch5NiW, and ChHANiW samples at all concentrations (2.5, 5, and 10%), while the others did not show statistically significant changes compared to the control. On day 14, the samples with the highest Ni concentration (Ch10NiW and ChHA10NiW) proved to be toxic, with metabolic activity values below 40%. Samples Ch2.5NiW, ChHA, and ChHA2.5NiW did not show statistically significant reductions compared to the control, while samples Ch, Ch5NiW, and ChHA5NiW showed a statistically significant reduction to approximately 80% of metabolic activity. For indirect contact (Fig. 5B) on day 1, a slight statistically significant reduction was observed for samples ChHA5NiW and ChHA10NiW, reaching values close to 80%. On day 3, samples Ch, ChNiW, and ChHANiW, with both 5% and 10% $NiWO_4$, showed a statistically significant reduction in metabolic activity, reaching values of 75%. On day 3, sample Ch2.5NiW also showed a slight statistically significant reduction, reaching values of 90%, while samples ChHA and ChHA2.5NiW showed no statistically significant difference from the control. On day 14, the Ch and ChHA samples showed no statistically significant differences compared to the control, while all other samples showed a slight statistically significant reduction, with metabolic activity values exceeding 80%. The toxicity of these scaffolds was also tested by direct contact with L929 cells (Fig. S5), showing a profile similar to that of MC3T3-E1 cells. These results show that indirect contact, *i.e.*, ion release of the ceramic or soluble components of chitosan, does not cause toxicity in MC3T3-E1 cells, while after 14 days of direct exposure to scaffolds with higher concentrations of $NiWO_4$ (Ch10NiW and ChHA10NiW),

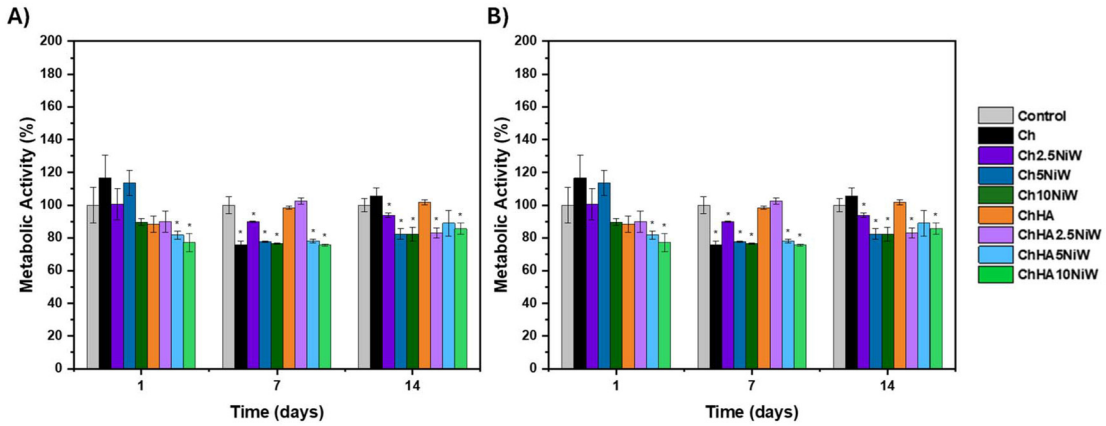

Fig. 5 Metabolic activity of MC3T3-E1 cells using rezausurine. (A) By direct contact and (B) by indirect contact. Results are presented as mean ± standard deviation (n = 9). Statistical analysis was performed using one-way ANOVA followed by a *post-hoc* test, with differences considered statistically significant when $*p < 0.05$.

toxicity is observed. A possible contributing factor is the release of Ni^{2+} ions combined with the semiconductor behavior of $NiWO_4$, which may promote surface redox reactions. Even under dark conditions, defect states at the material surface can interact with water molecules and dissolved oxygen, leading to the formation of highly reactive radical species.[39,71] These reactive intermediates may enhance oxidative stress in the surrounding microenvironment, contributing to the observed reduction in metabolic activity.

The oxidative and nitrosative stresses of MC3T3-E1 cells were analyzed through intracellular ROS production using the DCFDA probe and RNS production using the Griess reaction (Fig. 6). Regarding ROS production, a substantial statistically significant increase was observed on the first day for the ChNiW and ChHANiW samples with 5–10% $NiWO_4$, reaching values above 200% compared to the control, while the other samples showed a more controlled increase in intracellular ROS, reaching values close to 140%. This result indicates that, initially, contact with the scaffolds may induce adaptive oxidative stress, which is dependent on $NiWO_4$ concentration, probably due to the generation of extracellular ROS by this semiconductor. On day 7, regulation of these values was observed for practically all samples, generating a slight statistically significant increase in ROS production between 120 and 140%. On day 14, there is no significant change compared to the control, showing cellular adaptability. However, it should be noted that although the Ch10NiW and ChHA10NiW samples show intracellular ROS values without significant differences, these values are much higher than other samples, since while the others have cell viability above 80%, these two samples have values below 40%. Regarding RNS production, a milder and more gradual increase is generally observed for all samples at all experimental times, reaching values between 3 and 5 nM, while baseline values are close to 3 nM. Lee *et al.*

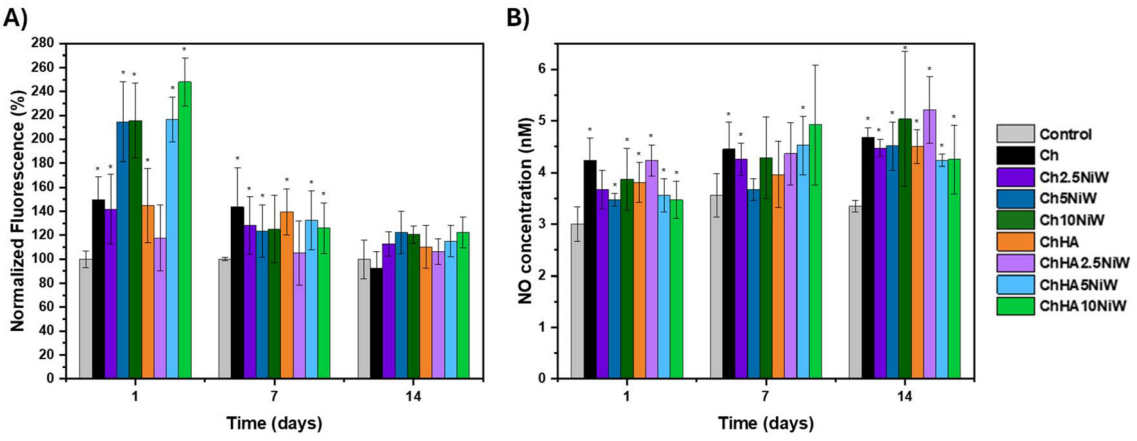

Fig. 6 Intracellular ROS and RNS production in MC3T3-E1 cells. (A) ROS production monitored by fluorescence using the DCFDA probe and (B) RNS production monitored by absorbance using the Griess reagent. Results are presented as mean ± standard deviation (n = 9). Statistical analysis was performed using one-way ANOVA followed by a *post hoc* test, with statistically significant differences considered at $p < 0.05$.

observed that NO levels in the range of 1 to 30 nM are considered biologically positive, being able to promote angiogenesis, cell survival and proliferation through the soluble guanylate cyclase (sGC) activation pathway.[72] These results corroborate those of Priya *et al.*, who doped hydroxyapatite with Ni^{2+}, improving its angiogenic properties.[34]

The wound healing assay (scratch) shown in Fig. 7 was performed to verify whether scaffolds can stimulate the migratory process of MC3T3-E1 cells after 24 and 48 h of exposure. Due to its cationic nature, chitosan is known to promote electrostatic interaction with the cell membrane which leads to initial adhesion as well as focal contacts necessary for motility.[73] Hydroxyapatite may even more intensify osteoblastic related reactions toward enhancing the orientation and migration of cells.[74] The cell migration results revealed a dose-dependent behavior in relation to the presence of $NiWO_4$. While the lowest concentrations (2.5% $NiWO_4$) promoted a significant increase in wound closure compared to the control, reaching approximately 40% in 48 h, the highest concentrations (10% $NiWO_4$) exerted an inhibitory effect. This phenomenon suggests that Ni^{2+} may exert a concentration-dependent biological effect within a narrow therapeutic window (<0.008 mM), above which metabolic inhibition can compromise cell motility. Similar behavior was reported by Liu *et al.*[75] in diabetic wound healing, where excessive and moderately prolonged oxidative stress impairs cell migration and tissue regeneration, while controlled bioactive stimuli can restore reparative pathways. Low concentrations of Ni^{2+} may modulate cellular redox signaling pathways rather than inducing overt oxidative damage. Transition metal ions at sub-toxic levels can participate in redox-sensitive signaling cascades, including the regulation of NF-κB, MAPK, and HIF-1α pathways, which are closely associated with cell migration, angiogenesis, and inflammatory modulation.[76] Within an appropriate thera-

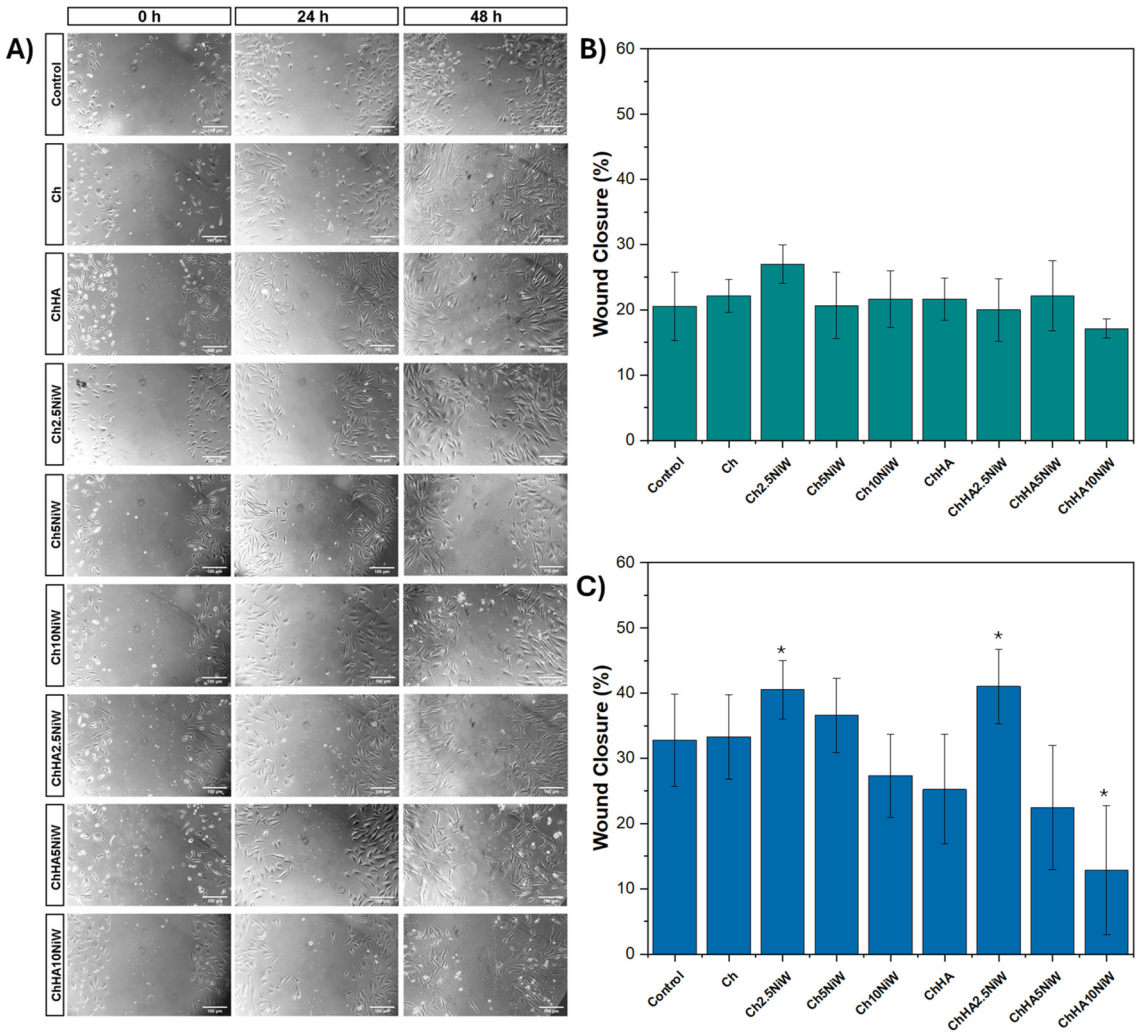

Fig. 7 Wound healing results (scratch assays) of the composite scaffolds using MC3T3-E1. (A) Images of the cell migration assay after 0, 24, and 48 h of exposure to the scaffold-conditioned medium. Quantification of wound closure corresponding to the images obtained in the cell migration assay at (B) 24 h and (C) 48 h. Results are presented as mean ± standard deviation (n = 3). Statistical significance was determined by one-way analysis of variance (ANOVA), followed by a *post hoc* test, with differences considered statistically significant when $*p < 0.05$.

peutic window, Ni^{2+} may contribute to the fine regulation of the redox microenvironment and inflammatory balance, thereby supporting cytoskeletal dynamics and directional cell migration. In contrast, excessive levels of Ni^{2+} can exacerbate metabolic stress, leading to mitochondrial dysfunction, increased ROS accumulation, and disruption of actin cytoskeleton organization compromising motility. Therefore, optimizing the Ni^{2+} content is essential to explore the beneficial biological effects of nickel while avoiding inhibitory responses.

To assess cellular mineralization capacity, an ARS staining assay was used after 7 and 14 days, identifying Ca deposits associated with osteogenic differentiation of MC3T3-E1 cells (Fig. 8). It is important to emphasize that the staining observed *via* ARS reflects cell-mediated mineralization and not merely the physicochemical precipitation of Ca^{2+} ions from the hydroxyapatite of the scaffolds. This biological process is characterized by the active secretion of matrix vesicles and the action of the alkaline phosphatase enzyme, which promotes the organized nucleation of apatite crystals on the newly synthesized collagen matrix, a definitive marker of the functional differentiation of MC3T3-E1 pre-osteoblasts.[77] Fig. 8A shows that, except for the Ch sample, after 7 days, all others show a statistically significant increase in osteogenic differentiation and mineral deposition, particularly the ChHA, Ch2.5NiW, and ChHA2.5NiW samples. Within 14 days, similar behavior occurs with the ChHA2.5NiW sample, showing greater osteogenic capacity. This can be confirmed by the photos of calcium deposits stained with ARS in Fig. 8B. These results agree with previous studies that have shown that the use of Ni^{2+} as a dopant in hydroxyapatite increases the capacity for osteogenic differentiation and increases mineral deposition.[33,34]

Confocal microscopy was used to investigate the adhesion profile and morphology of MC3T3-E1 cells on the scaffolds (Fig. 9). DAPI markers were used for the nuclei, and Alexa Fluor 488-phalloidin was used for the cytoskeleton. However, it was noted that DAPI showed non-specific affinity for the support, interacting directly with the scaffold matrix instead of being restricted to the cell nuclei. In contrast, phalloidin demonstrated high specificity, allowing clear visualization of the cytoskeleton organization and cell extension on the material surface. For the Ch sample, a dense cell population adhered to the scaffold surface was observed; however, the predominantly globular morphology suggests a state of cellular stress and limited cytoplasmic spreading. A similar phenomenon is observed in the Ch2.5NiW and Ch5NiW samples, which show a high number of cells but low filopodial extension. In contrast, the Ch10NiW sample exhibited a reduction in both cell density and affinity, with cells showing a strictly spherical morphology, confirming a low adhesion capacity in this sample. On the other hand, the ChHA group revealed a distinct scenario; in addition to high cellularity, the cells presented a fully spread phenotype, demonstrating that the incorporation of hydroxyapatite acts as a potent inducer of adhesion and anchoring of MC3T3-E1 pre-osteoblasts. This phenomenon was also observed by Fu *et al.*,[78] in which the cellular specifications in poly(lactic-*co*-glycolic) acid with hydroxyapatite carriers exhibited an increased level compared to the pure polymer, which is related to the rough surface and biocompatibility of HA, which can increase adhesion, routinization, and osteogenic division. The same is observed for the ChHA2.5NiW and ChHA5NiW samples, in contrast to the ChHA10NiW sample, where the globular morphology is once again observed. These results are consistent with those of metabolic activity and oxidative stress, showing that high concentrations of $NiWO_4$ are detrimental to cell development.

Antimicrobial evaluation against *S. aureus* and *E. coli* was performed as complementary evidence of the multifunctionality of the developed scaffolds, and the results are shown in Table 3. Sample Ch, as well as sample ChHA, did not demonstrate significant antimicrobial activity against *S. aureus* and *E. coli*, with microbial reductions below 30%, indicating that it is not sufficiently potent to be used alone for adequate infection control. On the other hand, the incorporation of $NiWO_4$

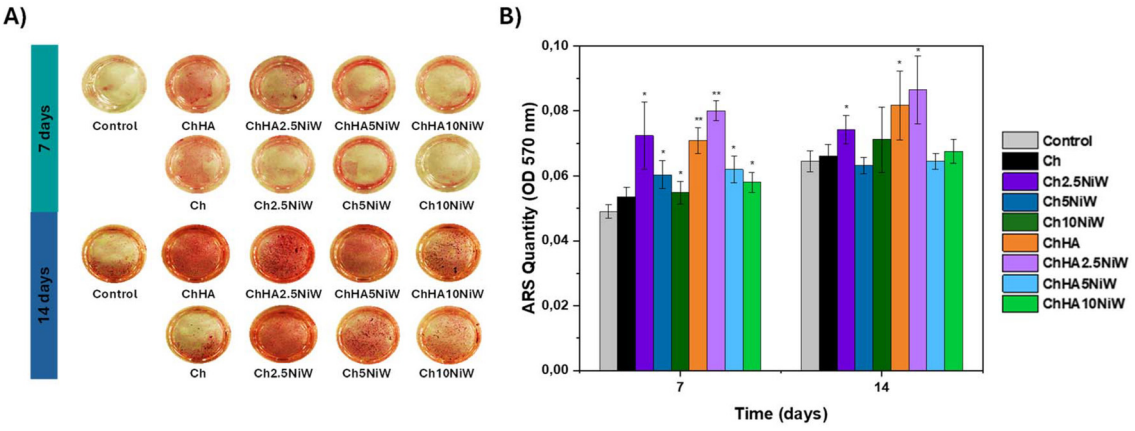

Fig. 8 Osteogenic differentiation of MC3T3-E1 cells using the ARS staining assay after 7 and 14 days. (A) Micrographs of the samples and (B) quantitative analysis. Results are presented as mean ± standard deviation (n = 3). Statistical significance was determined by one-way analysis of variance (ANOVA), followed by a *post hoc* test, with differences considered statistically significant when $*p < 0.05$.

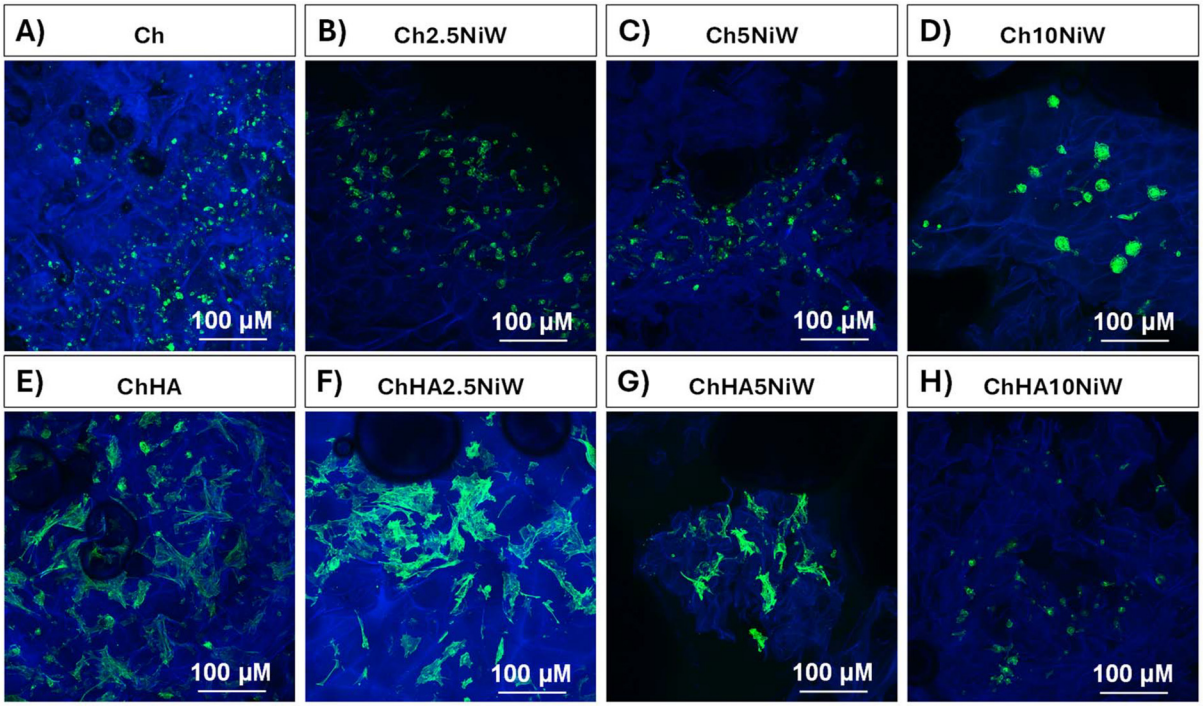

Fig. 9 Confocal optical microscopy images of adhered MC3T3-E1 cells after 1 day of contact, highlighting cytoskeletal organization visualized by phalloidin. Statistical significance was determined by one-way analysis of variance (ANOVA), followed by a *post hoc* test, with differences considered statistically significant when $*p < 0.05$.

significantly improved the antimicrobial performance in a dose-dependent manner, resulting in reductions greater than 80% for *S. aureus*, with the greatest reduction observed for sample Ch10NiW (98.3%). For *E. coli*, the antimicrobial performance values were greater than 95% for all samples, with sample Ch10NiW again standing out with a reduction of 99.3%. This behavior demonstrates that $NiWO_4$ is essential for bacterial suppression, likely through a mechanism related to membrane disruption and increased cellular stress due to the release of Ni^{2+} and ROS, with Gram-negative bacteria being more susceptible to its action due to the thinner membrane. Alshemary *et al.* observed that Ni^{2+}-doped hydroxyapatite increases the antimicrobial efficacy against *Pseudomonas aeruginosa* because of the interaction between Ni^{2+} and the charged phosphate and carboxylic groups of nucleic acids present on the surface of the bacteria, which results in the

Table 3 Antimicrobial activity of the composite scaffolds. Results are presented as mean ± standard deviation ($n = 3$). Statistical significance was determined by one-way analysis of variance (ANOVA), followed by a *post hoc* test, with differences considered statistically significant when $*p < 0.05$

	Sample	CFU mL^{-1}	Log reduction	% Inactivation
S. aureus	Control	$4.24 \times 10^7 \pm 2.39 \times 10^6$	—	—
	Ch	$2.99 \times 10^7 \pm 6.78 \times 10^5$*	0.15	29.48
	Ch2.5NiW	$4.22 \times 10^6 \pm 1.14 \times 10^6$*	1.00	90.05
	Ch5NiW	$1.23 \times 10^6 \pm 4.03 \times 10^5$*	1.54	97.10
	Ch10NiW	$7.25 \times 10^5 \pm 6.28 \times 10^4$*	1.77	98.29
	ChHA	$3.35 \times 10^7 \pm 2.46 \times 10^5$*	0.10	20.99
	ChHA2.5NiW	$7.33 \times 10^6 \pm 4.57 \times 10^5$*	0.76	82.71
	ChHA5NiW	$3.92 \times 10^6 \pm 1.08 \times 10^5$*	1.03	90.75
	ChHA10NiW	$9.39 \times 10^5 \pm 8.08 \times 10^4$*	1.65	97.78
E. coli	Control	$2.48 \times 10^8 \pm 2.95 \times 10^7$	—	—
	Ch	$1.97 \times 10^8 \pm 2.33 \times 10^6$*	0.10	20.56
	Ch2.5NiW	$9.08 \times 10^6 \pm 8.07 \times 10^5$*	1.44	96.34
	Ch5NiW	$5.22 \times 10^6 \pm 4.03 \times 10^5$*	1.68	97.89
	Ch10NiW	$1.71 \times 10^6 \pm 3.22 \times 10^5$*	2.16	99.31
	ChHA	$2.31 \times 10^8 \pm 1.12 \times 10^7$*	0.03	6.85
	ChHA2.5NiW	$1.22 \times 10^7 \pm 6.21 \times 10^6$*	1.31	95.08
	ChHA5NiW	$8.38 \times 10^6 \pm 7.18 \times 10^5$*	1.47	96.62
	ChHA10NiW	$5.69 \times 10^6 \pm 2.54 \times 10^5$*	1.64	97.70

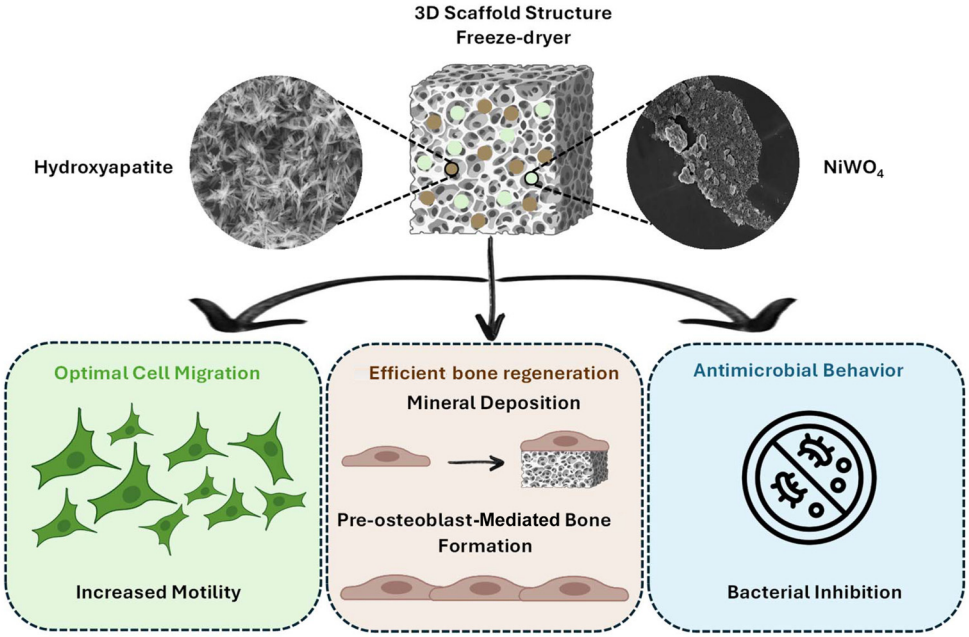

Fig. 10 Advantages for the use of freeze-dried scaffolds of chitosan with hydroxyapatite and $NiWO_4$.

inhibition of endogenous respiration in bacterial cells.[33] Karthiga *et al.* evaluated the antimicrobial activity of $NiWO_4$ nanoparticles, which are efficient against *S. aureus*, *Salmonella*, *Klebsiella pneumoniae* and *Aspergillus niger*, due to Ni^{2+} release and ROS production.[37]

In this sense, a synergy of effects is observed between chitosan, hydroxyapatite, and $NiWO_4$ (Fig. 10). While chitosan acts as a structural matrix for anchoring inorganic nanoparticles, hydroxyapatite increases the biocompatibility and cell adhesion without inducing significant oxidative stress. Simultaneously, low concentrations of $NiWO_4$ optimize cell mobility, enhancing cell migration, and demonstrate the potential to induce osteogenic differentiation of pre-osteoblasts by mineral deposition, in addition to conferring antimicrobial properties to the scaffold. By balancing physicochemical properties and bioactivity, the ChHA2.5NiW sample establishes itself as a promising candidate for applications in BTE.

4. Conclusions

The development of new biomaterials for BTE applications is constant. In this sense, hybrid materials with thoughtful compositions obtained through advanced manufacturing methodologies become potential candidates to successfully improve the tissue repair process. In this work, hybrid chitosan and hydroxyapatite scaffolds obtained by freeze-drying were reinforced with amorphous $NiWO_4$ semiconductor nanoparticles due to their ability to release Ni^{2+} in a controlled manner and produce ROS even in the dark. Structural and morphological analyses showed that the components are not degraded during manufacturing, but the synergy between the polymer and the inorganic fillers directly impacts their morphology and consequently their mechanical properties, stability, and release of Ca^{2+} and Ni^{2+} ions.

These hybrid scaffolds exhibit toxicity to MC3T3-E1 and L929 cells only at longer exposure times, with the highest concentrations of $NiWO_4$ (10%). Furthermore, it is observed that $NiWO_4$ is responsible for an increase in intracellular oxidative stress, which is regulated after an adaptive process in these cells. While chitosan provides all the essential structural support for the scaffold, hydroxyapatite improves its biocompatibility, in addition to inducing improvements in cell adhesion. Meanwhile, $NiWO_4$ could improve cell motility by increasing the migration rate, as well as inducing osteodifferentiation of MC3T3-E1 cells, which leads to an increase in the mineralization of Ca salts, evidenced by ARS tests. Due to the controlled release of Ni^{2+} and ROS, it is also possible to observe that these scaffolds have antimicrobial activity against Gram-positive (*S. aureus*) and Gram-negative (*E. coli*) bacteria, thus endowing multifunctionality to the scaffolds.

The ChHA2.5NiW sample (10% hydroxyapatite and 2.5% $NiWO_4$) has a lot of structural, morphological, and bioactive properties that make it a good candidate for use in BTE. It could be a multifunctional scaffold that combines bioactivity with controlled redox modulation. These results also indicate that nanostructured semiconductors could constitute a novel category of functional additives in tissue engineering platforms, extending beyond their conventional catalytic roles. Subsequent research will concentrate on clarifying the precise function of $NiWO_4$ in cellular metabolic pathways associated with proliferation, differentiation, and redox regulation, along with the development of more extensive *in vivo* models to

confirm the biological efficacy and long-term safety of these materials.

Author contributions

G. A. G.: conceptualization, methodology, investigation, data curation, formal validation, resources, visualization, writing – original draft, and writing – review & editing. D. G. N. N., K. S. J. S., and M. B.: methodology, investigation, data curation, and formal validation. A. S. A. and J. P. S. P.: methodology, investigation, and data curation. R. N. G., A. J. M., and A. C. M. R.: formal validation, resources, project administration, supervision, resources, and writing – review & editing. E. L. and M. A.: conceptualization, methodology, investigation, data curation, formal validation, resources, project administration, supervision, resources, writing – original draft, and writing – review & editing.

Conflicts of interest

There are no conflicts to declare.

Data availability

Data for this article, including characterization and biological assay data, are available at Zenodo at https://doi.org/10.5281/zenodo.18364166.

Supplementary information (SI) is available. See DOI: https://doi.org/10.1039/d6bm00120c.

Acknowledgements

This work was supported by Fundação de Amparo à Pesquisa do Estado de São Paulo – FAPESP through grants no. #2013/07296-2, #2024/15977-4, #2024/19218-0, #2026/00695-9, #2024/11111-2, #2025/03246-8, #2022/13515-8, #2021/11845-8, and #2022/06219-3. The authors also acknowledge Coordenação de Aperfeiçoamento de Pessoal de Nível Superior – CAPES #001 and Conselho Nacional de Desenvolvimento Científico e Tecnológico – CNPq for financial support.

References

1 V. T. Hoang, Q. T. Nguyen, T. T. K. Phan, T. H. Pham, N. T. H. Dinh, L. P. H. Anh, L. T. M. Dao, V. D. Bui, H. Dao, D. S. Le, A. T. L. Ngo, Q. Le and L. N. Thanh, *MedComm*, 2025, **6**, e70192.
2 S. Z. Jalise, A. Mehrabi, S. Habibi, P. B. Milan and A. Rezapour, *Polym. Adv. Technol.*, 2025, **36**, e70152.
3 A. A. Golebiowska, J. T. Intravaia, V. M. Sathe, S. G. Kumbar and S. P. Nukavarapu, *Bioact. Mater.*, 2024, **32**, 98–123.
4 Y. Chen, X. Dong, M. Shafiq, G. Myles, N. Radacsi and X. Mo, *Adv. Fiber Mater.*, 2022, **4**, 959–986.
5 X. Chen, T. Wu, Y. Bu, H. Yan and Q. Lin, *Int. J. Mol. Sci.*, 2024, **25**, 7810.
6 C. Katrilaka, N. Karipidou, N. Petrou, C. Manglaris, G. Katrilakas, A. N. Tzavellas, M. Pitou, E. E. Tsiridis, T. Choli-Papadopoulou and A. Aggeli, *Materials*, 2023, **16**, 4425.
7 K. L. Scotti and D. C. Dunand, *Prog. Mater. Sci.*, 2018, **94**, 243–305.
8 J. Grenier, H. Duval, P. Lv, F. Barou, C. Le Guilcher, R. Aid, B. David and D. Letourneur, *Biomater. Adv.*, 2022, **139**, 212973.
9 N. Angraini, S. Syarifuddin, N. Rauf and D. Tahir, *Artif. Organs*, 2025, **49**, 1236–1248.
10 S. V. Agocsova, M. Culenova, I. Birova, L. Omanikova, B. Moncmanova, L. Danisovic, S. Ziaran, D. Bakos and P. Alexy, *Materials*, 2023, **16**, 4267.
11 C. J. Agnes, A. Karoichan and M. Tabrizian, *ACS Appl. Bio Mater.*, 2023, **6**, 2515–2545.
12 H. Aksel, F. Mahjour, F. Bosaid, S. Calamak and A. A. Azim, *J. Endod.*, 2020, **46**, 1867–1875.
13 M. Bonifacio, C. C. S. Martignago, D. C. S. Souza, H. Garcia-Motta, L. C. Souza-Silva, B. Soares-Silva, K. S. J. Sousa, A. P. Rosso, J. H. G. Lago, A. M. Ribeiro, M. Assis, R. N. Granito and A. Rennó, *ACS Omega*, 2025, **10**, 25605–25620.
14 M. Assis, M. Gutiérrez-Blanco, F. Lipsky, L. K. Ribeiro, M. Martí, A. Cano-Vicent, M. A. San-Miguel, R. Llusar, J. Andrés, A. C. M. Rennó and A. Serrano-Aroca, *ACS Appl. Polym. Mater.*, 2025, **7**, 16011–16029.
15 L. Signorini, G. Marenzi, A. Facente, B. Marrelli, R. M. Marano, A. Valletta, L. Pacifici, R. Gasparro, G. Sammartino and M. Severino, *Int. J. Med. Sci.*, 2023, **20**, 1527–1534.
16 J. Rahaman, A. Reza, D. Nasare, J. Susanth and D. Mukherjee, *Mater. Today Commun.*, 2025, **49**, 113948.
17 K. Jahan, M. Mekhail and M. Tabrizian, *Carbohydr. Polym.*, 2019, **203**, 60–70.
18 P. J. Piszko, A. Piszko, S. Kiryk, J. Kiryk, T. Horodniczy, N. Struzik, K. Wiśniewska, J. Matys and M. Dobrzyński, *Biomimetics*, 2024, **9**, 503.
19 D.-E. Radulescu, O. R. Vasile, E. Andronescu and A. Ficai, *Int. J. Mol. Sci.*, 2023, **24**, 13157.
20 N. Rezania, M. Asadi-Eydivand, N. Abolfathi, S. Bonakdar, M. Mehrjoo and M. Solati-Hashjin, *J. Mater. Sci. Mater. Med.*, 2022, **33**, 31.
21 X. Mo, D. Zhang, K. Liu, X. Zhao, X. Li and W. Wang, *Int. J. Mol. Sci.*, 2023, **24**, 1291.
22 S. Soleymani and S. M. Naghib, *Heliyon*, 2023, **9**, e19363.
23 N. A. A. Halim, M. Z. Hussein and M. K. Kandar, *Int. J. Nanomed.*, 2021, **16**, 6477–6496.
24 J. S. Silva, T. R. Machado, T. A. Martins, M. Assis, C. C. Foggi, N. G. Macedo, H. Beltrán-Mir, E. Cordoncillo, J. Andrés and E. Longo, *Inorg. Chem.*, 2019, **58**, 5900–5913.

25 W. Zhou, Z. Hu, T. Wang, G. Yang, W. Xi, Y. Gan, W. Lu and J. Hu, *Colloids Surf., B*, 2020, **186**, 110710.
26 S. Panda, C. K. Biswas and S. Paul, *Ceram. Int.*, 2021, **47**, 28122–28144.
27 H. Shi, Z. Zhou, W. Li, Y. Fan, Z. Li and J. Wei, *Crystals*, 2021, **11**, 149.
28 A. Z. Alshemary, M. Akram, Y.-F. Goh, U. Tariq, F. K. Butt, A. Abdolahi and R. Hussain, *Ceram. Int.*, 2015, **41**, 11886–11898.
29 C. B. de Abreu, R. C. Gebara, G. S. Rocha, A. S. Mansano, M. Assis, T. M. Pereira, L. S. Virtuoso, A. J. Moreira, M. A. Santos, M. d. G. G. Melão and E. Longo, *Int. Microbiol.*, 2025, **28**, 1449–1461.
30 M. Horie, K. Nishio, K. Fujita, H. Kato, A. Nakamura, S. Kinugasa, S. Endoh, A. Miyauchi, K. Yamamoto, H. Murayama, E. Niki, H. Iwahashi, Y. Yoshida and J. Nakanishi, *Chem. Res. Toxicol.*, 2009, **22**, 1415–1426.
31 S. R. de Annunzio, M. Assis, P. A. Barbugli, A. S. Rosa, T. K. F. Oliveira, T. A. N. Quintão, V. N. d. S. Ferreira, T. d. E. Sá-Guimarães, G. B. da Conceição, D. F. Barreto-Vieira, R. D. Piazza, R. F. C. Marques, M. D. Miranda, E. Longo and C. E. Vergani, *ACS Omega*, 2025, **10**, 58975–58990.
32 M. Assis, J. R. Santos, M. H. L. Cipriano, R. Y. N. Reis, L. K. Ribeiro, L. H. Mascaro, E. Longo and J. Andrés, *Surf. Interfaces*, 2024, **53**, 105074.
33 A. Z. Alshemary, M. Akram, Y.-F. Goh, U. Tariq, F. K. Butt, A. Abdolahi and R. Hussain, *Ceram. Int.*, 2015, **41**, 11886–11898.
34 B. A. Priya, K. Senthilguru, T. Agarwal, S. N. G. H. Narayana, S. Giri, K. Pramanik, K. Pal and I. Banerjee, *RSC Adv.*, 2015, **5**, 72515–72528.
35 M. Assis, A. Cano-Vicent, A. Tuñon-Molina, J. Andrés and A. Serrano-Aroca, *Mater. Res. Bull.*, 2026, **195**, 113856.
36 C. B. de Abreu, R. C. Gebara, T. T. Dorini, G. S. Rocha, A. d. S. Mansano, M. Assis, T. M. Pereira, L. S. Virtuoso, M. A. San-Miguel, M. d. G. G. Melão and E. Longo, *ACS Omega*, 2025, **10**, 59413–59424.
37 R. Karthiga, B. Kavitha, M. Rajarajan and A. Suganthi, *Mater. Sci. Semicond. Process.*, 2015, **40**, 123–129.
38 P. Selvakumar, S. Thiyagarajan, S. Ganesan and S. Calisius, *Eur. Phys. J. Plus*, 2025, **140**, 651.
39 P. Selvakumar and S. Thiyagarajan, *J. Alloys Compd.*, 2025, **1048**, 185323.
40 G. A. Grasser, L. K. Ribeiro, E. Longo and M. Assis, *Catal. Today*, 2025, **444**, 114999.
41 T. R. Machado, J. C. Sczancoski, H. Beltrán-Mir, I. C. Nogueira, M. S. Li, J. Andrés, E. Cordoncillo and E. Longo, *J. Solid State Chem.*, 2017, **249**, 64–69.
42 K. S. J. Sousa, A. de Souza, M. A. Cruz, L. E. de Lima, G. E. Santo, G. O. Amaral, R. N. Granito and A. C. Renno, *Bioprocess Biosyst. Eng.*, 2024, **47**, 1483–1498.
43 M. Assis, A. de Souza, K. S. J. Sousa, D. G. N. Nina, M. Bonfacio, R. N. Granito and A. C. M. Rennó, *J. Appl. Toxicol.*, 2025, **45**, 2197–2216.
44 M. Assis, A. Cano-Vicent, A. Tuñon-Molina, R. R. Benzi-Chumachenco, J. Andrés and A. Serrano-Aroca, *J. Environ. Chem. Eng.*, 2024, **12**, 113935.
45 R. M. Wilson, J. C. Elliott and S. E. P. Dowker, *Am. Mineral.*, 1999, **84**, 1406–1414.
46 A. Kumaresan, A. Arun, V. Kalpana, P. Vinupritha and E. Sundaravadivel, *J. Mater. Sci.: Mater. Electron.*, 2022, **33**, 9660–9668.
47 N. Keanjun, T. Rattanawongwiboon, P. Sricharoen, S. Laksee, N. Saengsane, Y. Thepchuay, P. Porrawatkul, R. Pimsen, A. Kuyyogsuy, P. Nuengmatcha, S. Chanthai, M. Subsadsana and N. Limchoowong, *RSC Adv.*, 2024, **14**, 29737–29747.
48 L. O. Libero, L. K. Ribeiro, L. I. Granone, M. S. Churio, J. C. Souza, V. R. Mastelaro, J. Andrés, E. Longo, L. H. Mascaro and M. Assis, *ChemCatChem*, 2023, **15**, e202300421.
49 G. Hao, Y. Hu, L. Shi, J. Chen, A. Cui, W. Weng and K. Osako, *Sci. Rep.*, 2021, **11**, 1646.
50 S. J. d. M. Alves, M. A. Santos, J. E. d. S. Neto, H. N. da Silva, M. C. d. S. Barbosa, M. V. L. Fook, R. F. Navarro and S. M. d. L. Silva, *Gels*, 2025, **11**, 212.
51 G. P. Parchen, M. Quaillet, R. A. Freitas and H. Hillaireau, *RSC Pharm.*, 2025, **2**, 1292–1322.
52 C. Ardean, C. M. Davidescu, N. S. Nemeș, A. Negrea, M. Ciopec, N. Duteanu, P. Negrea, D. Duda-Seiman and V. Musta, *Int. J. Mol. Sci.*, 2021, **22**, 7449.
53 Y. Chen, A. Etxabide, A. Seyfoddin and M. Ramezani, *Mater. Today Proc.*, 2023, DOI: 10.1016/j.matpr.2023.02.303.
54 C. Torres, O. Valerio, R. T. Mendonça and M. Pereira, *Int. J. Biol. Macromol.*, 2024, **267**, 131587.
55 R. Ruiz-Caro and M. D. Veiga-Ochoa, *Molecules*, 2009, **14**, 4370–4386.
56 S. Ghaziof, S. Shojaei, M. Mehdikhani, M. Khodaei and M. J. Nodoushan, *J. Mech. Behav. Biomed. Mater.*, 2022, **132**, 105271.
57 J. Grenier, H. Duval, F. Barou, P. Lv, B. David and D. Letourneur, *Acta Biomater.*, 2019, **94**, 195–203.
58 H. Zhang, C. Liu, L. Chen and B. Dai, *Chem. Eng. Sci.*, 2019, **201**, 50–57.
59 A. F. N. Navas, D. G. Araujo-Rodríguez, C.-H. Valencia-Llano, D. Insuasty, J. Delgado-Ospina, D. P. Navia-Porras, P. A. Zapata, A. Albis and C. D. Grande-Tovar, *Molecules*, 2024, **29**, 3850.
60 J. Liang, Y. Wu, Z. Huang, F. Feng, M. Wei and J. Wu, *Discover Appl. Sci.*, 2024, **6**, 652.
61 N. Angraini, S. Syarifuddin, N. Rauf and D. Tahir, *Artif. Organs*, 2025, **49**, 1236–1248.
62 J. Gonçalves, M. L. Pinto, P. Ferreira and C. Nunes, *Carbohydr. Polym.*, 2025, **368**, 124207.
63 N. Abdian, M. Etminanfar, S. O. R. Sheykholeslami, H. Hamishehkar and J. Khalil-Allafi, *Mater. Chem. Phys.*, 2023, **301**, 127672.
64 E. F. dos Santos, L. R. Lourenço, C. A. da Silva and J. Marchi, *ACS Omega*, 2025, **10**, 48500–48513.

65 C. O. Correia, Á. J. Leite and J. F. Mano, *Carbohydr. Polym.*, 2015, **123**, 39–45.
66 A. Dridi, K. Z. Riahi and S. Somrani, *J. Phys. Chem. Solids*, 2021, **156**, 110122.
67 C. Garbo, J. Locs, M. D'Este, G. Demazeau, A. Mocanu, C. Roman, O. Horovitz and M. Tomoaia-Cotisel, *Int. J. Nanomed.*, 2020, **15**, 1037–1058.
68 M. Taira, M. S. Toguchi, Y. Hamada, J. Takahashi, R. Itou, S. Toyosawa, N. Ijyuin and M. Okazaki, *J. Mater. Sci. Mater. Med.*, 2001, **12**, 373–376.
69 T.-T. Li, Y. Zhang, H.-T. Ren, H.-K. Peng, C.-W. Lou and J.-H. Lin, *Carbohydr. Polym.*, 2021, **260**, 117765.
70 N. Abdian, H. S. Zangbar, M. Etminanfar and H. Hamishehkar, *Int. J. Biol. Macromol.*, 2024, **278**, 135014.
71 A. F. Gouveia, M. Assis, L. K. Ribeiro, E. d. O. Gomes, M. D. Teodoro, E. Longo and J. Andrés, *J. Mater. Chem. C*, 2025, **13**, 6788–6798.
72 J. Lee, D. Kim, S. Park, S. Baek, J. Jung, T. Kim and D. K. Han, *Adv. Sci.*, 2023, **10**, 2205336.
73 S. Pramanik, A. Aggarwal, A. Kadi, M. Alhomrani, A. S. Alamri, W. F. Alsanie, K. Koul, A. Deepak and S. Bellucci, *RSC Adv.*, 2024, **14**, 19219–19256.
74 Z. Sabouri, M. Dequeecker, H. Anees, F. R. Adib, R. Jamous, J. Zheng, X. Lyu, S. Stötzel, C. Heiß, T. El Khassawna and V. Jahed, *Mater. Today Bio*, 2025, 102685.
75 J. Liu, Z. Chen, H. Liu, S. Qin, M. Li, L. Shi, C. Zhou, T. Liao, C. Li, Q. Lv, M. Liu, M. Zou, Y. Deng, Z. Wang and L. Wang, *Small*, 2024, **20**, 2305076.
76 S. Das, R. C. Reddy, K. S. Chadchan, A. J. Patil, M. S. Biradar and K. K. Das, *Endocr., Metab. Immune Disord.: Drug Targets*, 2020, **20**, 1024–1031.
77 A. Bernar, J. V. Gebetsberger, M. Bauer, W. Streif and M. Schirmer, *Int. J. Mol. Sci.*, 2022, **24**, 723.
78 C. Fu, X. Yang, S. Tan and L. Song, *Sci. Rep.*, 2017, **7**, 12549.